Aspects of Flow Characteristics and Turbulence in Complex Terrain

Results from the MAP-RIVIERA project

Inauguraldissertation

zur Erlangung der Würde eines Doktors der Philosophie

vorgelegt der Philosophisch-Naturwissenschaftlichen Fakultät

der Universität Basel von

Eva van Gorsel

aus Pfeffikon (Luzern)

Basel, 2003

Genehmigt von der Philosophisch- Naturwissenschaftlichen Fakultät der Universität Basel auf Antrag der Herren Professoren Eberhard Parlow, Basel, und Christian Bernhofer, Dresden.

Basel, den 18.06.2003

Prof. Dr. M. Tanner
Dekan

Acknowledgement

First of all I would like to thank Prof. Dr. Eberhard Parlow for giving me the opportunity to write this thesis at the Institute of Meteorology, Climatology and Remote Sensing at the University of Basel. At the institute there is not only a high technical standard which eases work, but there is also an extremely motivating atmosphere.

Thanks to Dr. Roland Vogt the MCR-Lab participated in the MAP-RIVIERA project. I would like to thank him for the confidence he had in my abilities to cope with the requirements inherent in such an experiment. I appreciated that he always handed his skills over, be it in scientific questions or in measurement techniques. It was great to get opportunities to participate at different experiments and to attend workshops and courses. Discussions about work were always an enjoyable challenge, fruitful and inspiring and I hope that they will go on in the future.

Special thanks go to Andreas Christen. He accompanied the whole project and contributed many ideas and results. Without his support we would not have been able to carry out all those measurements. Especially station F1 would never have been built. Mentioning station F1: thanks also to Florian Imbery and Mathias Müller for the days we spent building up the three F-stations and of course for all the work done during this time.

Many students helped setting up and tearing down towers: Sven Bethke, Andreas Christen, Andi Felber, Claudius Heinemann, Florian Imbery, Peter Keller, Eliane Müller and Matthias Müller. Thanks to all of them.

Dr. Norbert Kalthoff of the FZ Karlsruhe, and Prof. Dr. Andrea Pitacco of the University of Padova helped with instruments.

Essentially all members of the MCR-Lab gave support, contributed and exchanged ideas. When Günter Bing is around computers usually do what they are supposed to do. And if on rare occasions they don't he always has some advise. Dr. Christian Feigenwinter was always ready to help when I got stuck in some incoherency. Sharing a room implicates listening to many new born ideas of the other. That was Irene Lehner's lot. Thanks for the many discussions, critics, hints and chocolate. I would like to thank Paul Müller who prepared a lot of mounting devices for the instruments and always gave a helping hand when technical questions arose.

The collaborations with members of the ETHZ was also a precious help: thanks to Marco Andretta, Pierluigi Calanca, Petra Klein, Natascha Kljun, Mathias Rotach and Alexandra Weiss. Special thanks go to Karl Schroff for discussions and support in Campbell programming.

Manuel Pfeiffer always supported my work. Our friendship helped me through the more difficult phases of this thesis.

I would like to acknowledge the financing of this study by the Swiss National Science Foundation #21-055874.98 and #21-054060.98.

Zusammenfassung

In dieser Arbeit werden Turbulezmessungen aus dem MAP-RIVIERA Projekt analysiert. Während des Projektes wurden mehrere permanente Turbulenzmessstationen betrieben, die in einem Querschnitt durch das Riviera Tal aufgebaut waren. Weiter wurden Messungen von z.B. Radiosonden und einem Temperaturprofilgerät während Intensivmessperioden durchgeführt.

Da grosse Anteile der Alpen bewaldet sind, wurde ein Mast mit u.a. sechs Turbulenzmessniveaus in einem Mischwald am Hang (35°) montiert. Die Daten werden mit Studien aus Wäldern in idealerem Gelände verglichen. 30 min Statistiken, Wahrscheinlichkeitsdichteverteilungen, Längenskalen, und spektrale Eigenschaften werden diskutiert, kohärente Strukturen und ihre Zeitskalen aufgezeigt und Flussanteile, die sie bewirken, dargestellt.

Thermisch induzierte Hang- und Talwinde interagieren auf unterschiedlichen räumlichen und zeitlichen Skalen. Dies führt zu komplexen Impulstransporten. Letztere unterscheiden sich stark von dem, was aus *surface layer* Messungen bekannt ist. Windrichtungsscherung bewirkt laterale Transporte der gleichen Grössenordnung, wie sie die longitudinalen aufweisen. Im Bestand kommt es zu einer starken Reduktion der Turbulenz. Die Verteilungen der Geschwindigkeitskomponenten sind schief, was auf intermittente Turbulenz hinweist. Über dem Bestand wird in der Abwesenheit von Wellen Energie aus der mittleren Strömung in kohärente *eddies* überführt. Die Längenskalen der Störungen sind mit denen aus anderen Beständen mittlerer Dichte vergleichbar. Im Bestand wird von der Strömung Arbeit gegen den Druck- und gegen den reibungsbedingten Widerstand des Bestandes selbst verrichtet. Kinetische Energie wird in kleinskalige Turbulenz des Strömungsnachlaufs und in Wärme überführt.

Wellenartige Strukturen treten in der stabilen Grenzschicht häufig auf. In der Talatmosphäre werden Temperaturschwankungen beobachtet, welche durch das gesamte Messvolumen in Phase sind, was auf topographisch ausgelöste Wellen hinweist. Die periodischen Oszillationen sind nicht nur auf die Talatmosphäre beschränkt, sondern werden mit einem Phasenversatz auch am Hang beobachtet. Das bewirkt, dass Windfeldveränderungen aufgrund von kompressionsbedingter Erwärmung verstärkt, oder sogar ausgelöst werden. Die nicht zeitgleiche periodische Erwärmung führt zu einem Zyklus, in dem (relativ kalte) Luft über dem Bestand hangaufwärts advektiert wird, während im Bestand die Kaltluft verlangsamt abfliesst. Wenn über dem Bestand Hangabwinde auftreten, wird warme Luft in den Bestand gemischt. Dieser Effekt ist gerade vor dem nächsten Drehen der Windrichtung am stärksten.

Summary

In this thesis turbulence measurements from the MAP-RIVIERA project are analysed. During the project a number of permanent turbulence stations were installed on a cross section of the Riviera valley. Furthermore measurements from e.g. radio sounding systems and a passive microwave profiler were carried out during intensive observation periods.

As large fractions of the alps are forested, a tower with amongst others six levels of ultrasonic anemometer thermometers was installed in a mixed forest at the slope (35°). This data set is compared to studies carried out over forests in more ideal, flat terrain. The analysis is carried out for 30 min mean data, joint probability distributions, length scales and spectral characteristics. Furthermore patterns of coherent structures are determined and dominating time scales as well as flux fractions are calculated.

Thermally induced slope and valley winds are interacting on different spatial and time scales leading to complex patterns in momentum transport which differ significantly from surface layer characteristics. Directional shear causes lateral momentum transports that are in the same order as the longitudinal ones. In the canopy a sharp attenuation of turbulence is observed. Skewed distributions of velocity components indicate that intermittent turbulent transports play an important role in the energy distribution. In the absence of larger scale waves energy is removed from the mean flow above the canopy and injected into coherent eddies. Length scales of these disturbances are comparable to those in forests in flat terrain. In the canopy work is done against pressure drag and against the viscous component of canopy drag. Kinetic energy is converted into fine scale wake turbulence and heat leading to vanishing second moments.

It is shown that wave like structures are a very common feature of the stable boundary layer. In the valley atmosphere temperature fluctuations are observed which are in phase through the whole measured layer indicating terrain generated waves. These temperature oscillations are not confined to the valley centre but they are also observed on stations at the slope. Having a phase shift between valley and slope oscillations it is proposed that terrain generated waves back up or even enable the mechanism of compressional warming on the valley slopes. It is shown, that due to compressional warming a cycle is initiated in which (relatively colder) air is advected slope upwards above the canopy while in the canopy (relatively warmer) air drains at low speed. When the downslope winds occur above the canopy relatively warmer air is mixed into the canopy. This effect is strongest just before the onset of a new ´upslope event´.

Table of contents

Figures

Tables

Symbols

a	leaf area per unit volume
A	energy density of amplitude spectrum
C	drag coefficient cospectral energy density
$E(\kappa)$	three dimensional velocity spectrum
$F(ii)$	one dimensional velocity spectra
f	cyclic frequency
g	acceleration due to gravity
h	canopy height
k	von Karman konstant
L	Monin Obukhov length
L_s	shear length scale
$L_{u,v,w}$	length scale of respective variable
p	pressure
P	joint probability phase angle
q	specific humidity
r	correlation coefficient
$Sk_{u,v,w}$	skewness of respective variable
S	spectral energy density
t	time
T	temperature
$\boldsymbol{U}$	wind vector
u, v, w	longitudinal, lateral and vertical wind component
U_c	convection velocity
u_s	slope wind component
u_*	friction velocity
$\overline{u'w'}$	kinematic flux of longitudinal momentum
v_s	valley wind component
$\overline{v'w'}$	kinematic flux of lateral momentum
$\overline{w'\theta'}$	kinematic heat flux
x, y, z	Cartesian coordinates
z	height above ground
z_i	depth of convective mixed layer
z_0	roughness length
δ_w	vorticity thickness
ε	turbulent energy dissipation rate
θ	potential temperature
θ_v	virtual potential temperature
θ_{sv}	sonic temperature
κ	wavenumber
λ	wavelet dilation
Λ_x	wavelength of coherent eddies
ρ	density
σ	standard deviation
τ	wavelet translation
ω	angular frequency
ξ	time lag
ψ	wavelet function

Abbreviations

CL	canopy layer
CWT	continuous wavelet transform
DWT	discrete wavelet transform
KE	kinetic energy
PBL	planetary boundary layer
SL	surface layer
Ri	Richardson number
Ri_c	critical Richardson number
TKE	turbulent kinetic energy

1 Introduction

Imporant parts of the Earth's surface are characterised by hills, valleys and mountains on a range of scales. They have a large impact on weather and climate. Topography strongly modulates the exchange of energy and momentum between surface and adjacent atmosphere. In a valley modifications of turbulent fluxes result not only from changes in surface properties such as roughness changes and varying surface cover but also from topographical properties such as azimuth and inclination of the slope and varying sky view factors. Terrain characteristics modify dynamically driven flows on different scales and induce thermally forced ones. Due to the difficulty that several complicating factors are met in the boundary layer above inclined surfaces, at present there exists little knowledge about the turbulence characteristics in mountainous terrain and possible parameterizations of exchange processes.

However in understanding flow over hills progress was made during the last decades (Wood, 2000). Jackson and Hunt (1975) initiated studies of turbulent flow over low hills in the boundary layer with a linear analysis. Predictions of the analysis were verified in several field campaigns (e.g. Bradley, 1980; Mason and King, 1985; Taylor and Teunissen, 1987) and wind tunnel studies (Finnigan et al., 1990). The latter were also applied for clarifying the role of additional roughness introduced by plant canopies (Finnigan and Brunet, 1995).

In order to get more information about boundary layer characteristics in mountainous terrain an extensive data set was gathered during the MAP-RIVIERA project. Measurements were carried out in the Riviera valley, in an alpine region in the southern part of Switzerland. Permanent turbulence measurements were carried out on a cross section in the Riviera valley and additional measurements were performed during Special Observing Periods (Rotach et al., 2002). However, for the questions addressed in this thesis, which are outlined below, only a small fraction of all available data were necessary and therefore used. In Section 3 a description of the sites and the measurements used for the analysis are given.

In section 2 a short introduction to the most important concepts of boundary layers in homogeneous terrain is given. As measurements carried out during MAP-RIVIERA were taken above rough surfaces in complex terrain, current knowledge about turbulence in and above plant canopies as well as about turbulence in non flat terrain is summarised.

Section 4 first gives a short introduction into diurnal patterns and associated turbulence. Then the following questions are addressed:

Is it (to some extent) possible to apply current knowledge on turbulence (possibly in modified form) in extreme topography?
As a large fraction of the Swiss Southern Alps is forested section 4.2 concentrates on the analysis of a dataset measured above a forested slope. Turbulence structure in and above forests in flat / homogeneous terrain is fairly well understood. Comparison of the experimental data with canopy layer / mixing layer theory gives an impression on how dominantly the plant canopy is responsible for the turbulence structure and how it is modified by topography. Single point statist7ics, joint probability distributions and spectral properties are compared with results obtained in studies treating canopy turbulence in flat terrain.

Shear flows are usually characterised by organised motions. Do topographically induced pressure distributions alter wind profiles such that these structures are inhibited or magnified? Sections 4.2.3 and 4.3.1 concentrate on the description of coherent, organised motions. An attempt is made to clarify differences in the turbulent structure to other shear flows described in literature by discussing topographic influences.

One can expect, that in the stably stratified valley atmosphere topographically induced waves are observed. The topic of section 4.3.2 is the detection and description of wave like oscillations. It is shown how the valley atmosphere and slope flows interact.

2 Theory

2.1 The planetary boundary layer

Descriptions of the planetary boundary layer can be found in a number of textbooks. Therefore only the most relevant concepts are introduced here. Further information can be found e.g. in Arya (2001), Kaimal and Finnigan (1994), Stull (2000) and Stull (1988).

The formation of the planetary boundary layer (PBL) is a consequence of the interactions between the atmosphere and its underlying surface. The surface acts as a source or sink of energy and momentum to the atmosphere. The atmosphere provides the large scale environment which may modify the surface input over a wide range of values (Businger, 1982). According to thermodynamical properties the troposphere can be subdivided into free atmosphere and outer and an inner layer.

The free atmosphere is extending from the tropopause down to the outer layer (Fig 2.1). It is not influenced by surface properties such as roughness and is in near geostrophic balance. The PBL is the part of the troposphere that is affected by the presence of the earth's surface. In the outer layer the influence of friction increases with decreasing height and therefore the wind field is increasingly subgeostrophic. Vertical mixing is height dependent. This is contrary to the inner layer where shear stress and turbulent exchange of momentum and scalars vary only little with height. The flow is insensitive to the earth's rotation and the wind field is determined by the pressure gradient and surface friction. The region where characteristics of both, the outer and the inner layer, can be discerned is referred to as inertial sublayer. In the inertial sublayer vertical fluxes are approximately constant, the Coriolis force is negligible and dynamic pressure effects not relevant. The latter play a crucial role in the roughness sublayer turbulence, where the influence of the surface and roughness elements cause an essentially three dimensional flow.

The state of the atmosphere depends on the following variables: the wind vector $\boldsymbol{U}$ with its longitudinal, lateral and vertical component (u,v,w), temperature T, specific humidity q, pressure p and density ρ. How these variables depend on time (t) and space (x,y,z) can be described with the

- Equation of state (ideal gas law)

and the conservation equations of

- mass (continuity equation)
- momentum
- moisture and
- heat (first law of thermodynamics)

However the set of equations as a whole is so complex that no analytical solution can be found for boundary layer descriptions. Depending on the scale of interest and on the order of magnitude, terms may be neglected or need to be parameterised. Two assumptions that

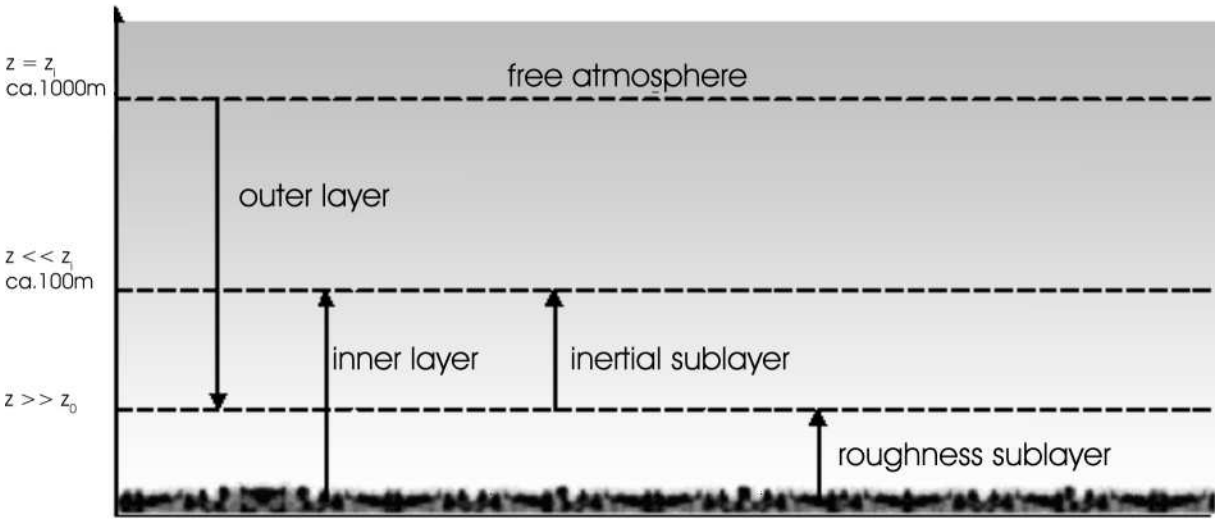

Fig 2.1: Schematic of the structure of troposphere and PBL (after e.g. Arya, 2001; Schmid and Rotach, 1997; modified).

lead to noticeable simplifications are specified here:

homogeneity: turbulent characteristics vary in the vertical only. In the horizontal they are constant and therefore the partial derivatives of mean quantities (the advection terms $\partial/\partial x$, $\partial/\partial y$) can be ignored along the horizontal axes. This assumption is valid if a 'required fetch' is present, where fetch refers to an upwind distance with uniform surface characteristics. This distance needs to be larger the higher measurements are carried out.

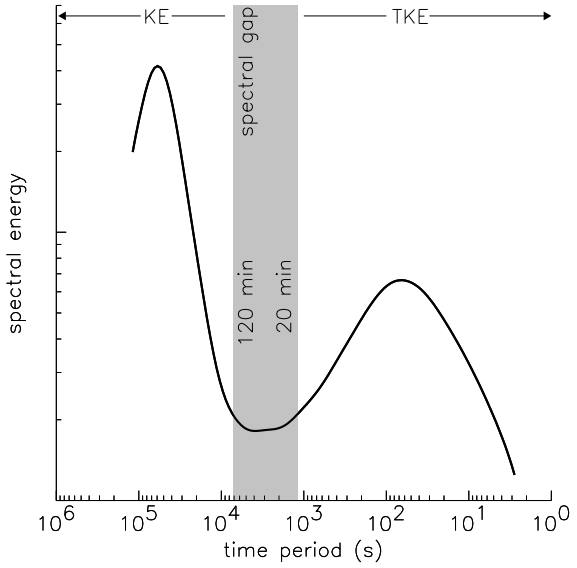

Fig 2.2: Distribution of spectral energy at different scales. (Global wavelet spectrum of (**T**urbulent) **K**inetic **E**nergy against Fourier period. Data (1 second block averages) are from station E2 at z/h = 1.74, September 8-15, 1999)

stationarity: turbulent characteristics do not vary in time ($\partial/\partial t = 0$). This assumption is never fulfilled in its narrower sense due to synoptic patterns and as essentially all meteorological variables show a diurnal cycle. However quasi stationary conditions can be achieved by choosing a suitable averaging time. This averaging time can be derived from the spectrum of atmospheric motions which fortunately often shows a gap at time periods of 20 minutes to 1 hour (Fig. 2.2). Therefore we have the possibility to isolate the large scale variations (which are here considered as instationarities) from the turbulent ones. The procedure with which this is achieved is called Reynolds decomposition. For any variable x we have

$$x(t) = \bar{x} + x'(t) \tag{2.1}$$

where

$$\bar{x} = \frac{1}{T_a}\int_0^{T_a} x(t)dt \tag{2.2}$$

is the average of $x(t)$ during the time interval T_a and $x'(t)$ is the deviation from this average.

A comprehensible overview on the governing equations, further assumptions with resulting applicable simplifications and rules on Reynolds averaging is given in Stull (1988).

boundary layer evolution: when the earth's surface is heated the lowest layers of the atmosphere often get unstable[1]. After sunrise a convective layer builds up. The PBL then is well

1 We can differentiate between static and dynamic stability: Stratification is considered statically stable if an overlying air mass is less dense (warmer, more humid) than the underlying one. However statically stable air can become turbulent if wind shear is strong enough. The Richardson number Ri indicates dynamic stability by relating the consumption or production of TKE by buoyancy (thermal turbulence) with the production of TKE by shear (mechanical turbulence).

$$Ri = \frac{\frac{g}{\bar{\theta}}\frac{\partial \bar{\theta}_v}{\partial z}}{\left(\frac{\partial \bar{u}}{\partial z}\right)^2 + \left(\frac{\partial \bar{v}}{\partial z}\right)^2} \tag{i}$$

Laminar flow becomes susceptible to the formation of Kelvin Helmholtz (KH) waves and the onset of turbulence if Ri is smaller than some critical threshold level Ri_c ($Ri_c \cong 0.25$). Small Ri indicate near neutral stability and mainly mechanical turbulence. If $\partial\theta_v/\partial z < 0$ any initial displacement of an air parcel is amplified and the stratification thus unstable. Large negative Ri indicate strong convection and negligible mechanical turbulence.

mixed due to turbulence. In the free atmosphere however the air is unmodified by turbulence. As a result there is often a sharp temperature increase in the transition zone between the two layers and only occasionally more energetic thermals penetrate this capping inversion. The convective layer and with it the capping inversion grows through the morning and may reach heights of 1-2 km in the afternoon. Towards the sunset the capping inversion weakens and shallow inversion layers build up. Turbulent motion weakens as the thermals lose their energy source. The air above the surface cools and is then mixed upwards by means of mechanical turbulence solely. The nocturnal stable boundary layer is much shallower (100-200 m) and is characterised by strong shear, intermittent winds and occasionally by wave activity.

2.1.1 Turbulence in plant canopies

During the last few decades many investigations were carried out in order to get a better knowledge of turbulence structure in and above plant canopies. Due to studies ranging from model canopies to horizontally homogeneous, flat forests a general few of canopy turbulence is now widely accepted and a 'family portrait' of the different experiments is depicted (Kaimal and Finnigan (1994); Raupach et al. (1996) and Raupach and Thom (1981)). A review on turbulence in plant canopies was recently given in Finnigan and Shaw (2000) and Finnigan and Brunet (1995).

In 1989 Raupach, Finningan and Brunet introduced the idea of comparing turbulence in vegetation canopies to turbulence in a plane mixing layer rather than to boundary layer turbulence. In their 1996 paper they wrote:"Our suggested analogy between mixing-layer and canopy turbulence flies in the face of a long-held view that canopy turbulence is a perturbed version of the turbulence in the overlying boundary layer. … [This view] ignores the basic nature of the canopy velocity profile: typically, the mean velocity profile has a strong inflection point near the top of the canopy….We argue that the instability processes arising from this inflection are essentially similar to those in a mixing layer."

Inflected velocity profiles of a mixing layer are unstable to small perturbations resulting in Kelvin-Helmholtz type instabilities. These Kelvin-Helmholtz waves set the pattern for coherent eddies and determine the turbulence length scales. The scale of the shear, L_s, is independent of wind speed, depending only on canopy height h and density (aerodynamic drag). L_s is around 0.1 h, 0.5 h, and h in dense, moderate and sparse canopies, respectively.

Large eddies are practically horizontal at heights of h. According to Townsend's hypothesis (1961) these eddies do not contribute actively to vertical transfer close to the ground. But even though eddies with vertical length scales much larger than L_s do not contribute actively to vertical turbulent mixing, they can lead to intermittency. Large scale gusts increase the shear at canopy top above some threshold level and initiate wave packets of several canopy scale coherent motions. The coherent motions then have a common convection velocity U_c which presumably corresponds to the velocity of the gust which initiated the instability. Thus convective velocities exceed the mean wind velocity within and immediately above the canopy and change only little with height (Shaw et al., 1995).

Figure 2.3 shows a schematic of canopy layer turbulence. Λ_x is the mean streamwise periodicity between successive coherent eddies. It is proportional to the shear length scale. The proportionality factor – which can be interpreted as an equivalent inverse Strouhal number S_{tr} (Brunet and Irvine, 2000) – was found to be 8.1±0.3 in plant canopies, where the theoretical expectation from mixing layer values was ranging from 7 to 10. In plane mixing layers the Strouhal number is proportional to the peak frequency of the u spectrum and the local vorticity thickness (δ_w) and inverse proportional to the mean velocity U defined as the arithmetic mean of the free stream velocities. Here the Strouhal number relates the shear length scale with the wavelength of coherent eddies by

$$S_{tr} = \frac{L_s}{\Lambda_x} \equiv \frac{\delta_w}{f_{\max(u)} / U}. \qquad (2.3)$$

The spanwise length scales of coherent motions - deduced from an array of towers – is roughly three times smaller than Λ_x (Zhang et al., 1992).

In the roughness sublayer one observes periods of relatively low wind speed associated with upward moving air (ejections) alternating with periods of relatively high speed air moving downward (sweeps). While at the top of the roughness sublayer ejections and sweeps contribute a similar amount to the total momentum transport, one has consistently observed that close to the rough surface sweeps dominate. Therefore skewnesses of longitudinal and vertical velocity - which tend to go to zero well above the canopy - are of opposite sign at canopy top (with Sk_u being positive) and in the canopy.

While vertical velocity is in phase through the canopy, one has often observed a continuous slight phase shift of the streamwise and spanwise velocity signal as well as of scalars with decreasing height, indicating a structure tilted in upwind direction.

In the canopy however fluctuations in the longitudinal wind component occurred with a phase shift of a roughly half a wavelength to those at higher levels. Shaw and Zhang (1992) have measured that accelerations at the ground occurred simultaneous with measured pressure perturbations. Having

$$p \propto 2\rho \frac{\partial \overline{u}}{\partial z} \frac{\partial \overline{w}}{\partial z} \qquad (2.4)$$

positive pressure perturbations occur ahead of advancing microfronts, when w changes from negative to positive values, inducing streamwise accelerations in trunk space. Physically, the pressure distributions in the upper layers are resulting from a sudden convergence of the flow in the horizontal direction (Zhuang and Amiro, 1994).

Pressure perturbations spread at the speed of sound and by transporting TKE lead to a redistribution and an increase of the latter in trunk space. For momentum however the canopy acts as a sink. A rapid decrease of $-\overline{u'w'}$ is observed as momentum is absorbed as aerodynamic drag on the foliage. Large dissipation rates of TKE are observed; the energy is converted into heat.

Above the canopy – in the roughness sublayer – energy is removed from the mean flow and injected into coherent eddies. In the canopy work is done against aerodynamic drag, thus against pressure drag and against the viscous component of canopy drag. Kinetic energy is then directly converted into fine scale wake turbulence and heat, respectively. These processes extract energy from the mean flow and from eddies of all scales larger than the canopy elements. This continuous removal of energy from the eddy cascade leads to a violation of the assumptions leading to Kolmogorov's hypothesis (see section 2.2.3).

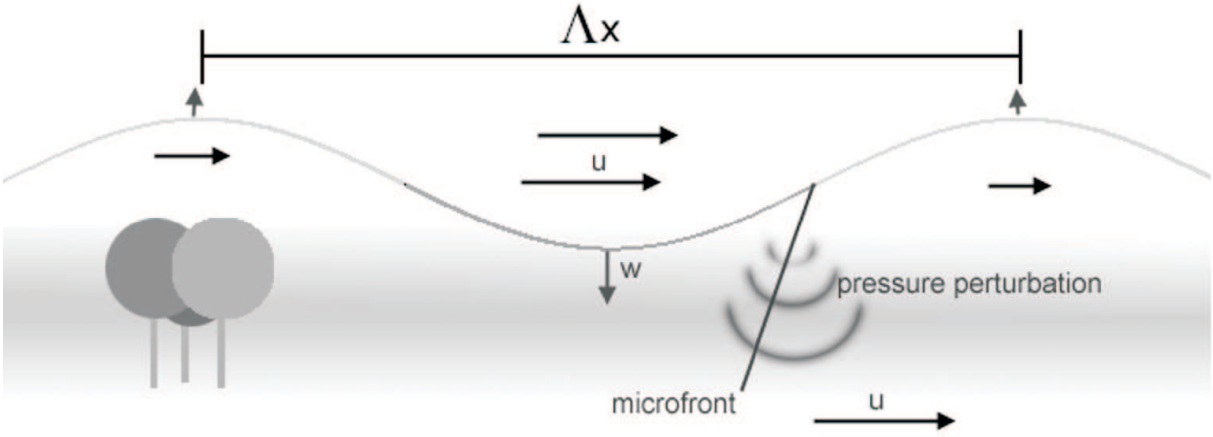

Fig 2.3: Schematic of canopy layer turbulence.

2.1.2 Turbulence and wave-like characteristics in complex terrain

Topography strongly modifies the exchange of energy and momentum between the Earth's surface and adjacent atmosphere. Modifications occur through a wide range of processes including radiative, thermodynamic and several dynamic flow effects (Raupach and Finnigan, 1997).

Topography can lead to mechanical blocking or channelling of the flow, and, apart from dynamic effects, topography determines the temporal and spatial distribution of radiation (Whiteman and Allwine, 1989). Different inclination and azimuth angles of surfaces lead to highly variable energy input, and radiative heating or cooling causes thermally induced circulations. While in mountainous terrain the mean wind field with local thermally induced circulation patterns is fairly well understood (e.g. Barry, 1992; Egger, 1990; Whiteman, 1990) there remains a lack of knowledge regarding turbulent exchange processes in mountainous regions (Rotach et al., 2000), as studies of turbulence in complex terrain are mainly restricted to hills so far (Wood, 2000). Here hills are defined as elevations that occupy only fractions of the PBL. In the following wind and turbulence over (forested) hills in a neutrally stratified atmosphere are described and a short description of katabatic winds in the stable boundary layer is given.

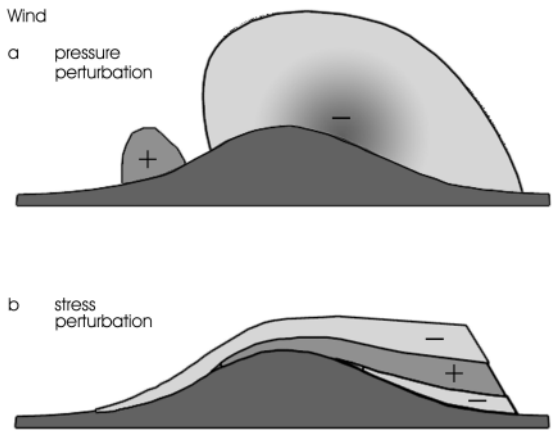

Fig. 2.4: Schematic diagrams of typical perturbations in a) pressure $p(x,z)$ and b) shear stress $\tau(x,z)$, for nonstratified flow over a low hill (from Raupach and Finnigan, 1997).

wind and turbulence over hills: the study of turbulent flow over hills in the boundary layer was initiated by Jackson and Hunt (1975). They developed a linear theory describing the flow over a hill of relatively low slope (< 26.6°) in a neutrally stratified boundary layer. They showed that a hill affects the velocity field by two mechanisms:

i by the pressure field around the hill and

ii by changes in the Reynolds stress.

If the atmosphere is neutrally stratified the momentum balance for flow over a laterally uniform ridge normal to the mean wind reads

$$\overline{u}\frac{\partial \overline{u}}{\partial x} + \overline{w}\frac{\partial \overline{w}}{\partial z} = -\frac{\partial p}{\partial x} + \frac{\partial \overline{u'w'}}{\partial z} \tag{2.5}$$

where x and z are Cartesian coordinates in streamwise and vertical direction respectively. As Fig. 2.4 shows a pressure perturbation field is set up when the flow goes over the hill, with positive deviations when the flow is approaching the hill and negative deviations in the lee of the obstacle. The momentum divergence originates at the surface and the perturbation diffuses upwards. The transport velocity is determined by turbulence itself (Raupach and Finnigan, 1997).

The flow can be divided in an inner and an outer region. In the outer region the perturbation turbulent stresses are negligible and the perturbed flow is nearly inviscid and irrotational. The momentum equation is a balance between acceleration and pressure gradient:

$$\overline{u}\frac{\partial \overline{u}}{\partial x} = -\frac{\partial p}{\partial x} \tag{2.6}$$

In the inner region the velocity field is modified by both pressure and the stress gradient such that the momentum balance reads:

$$\overline{u}\frac{\partial \overline{u}}{\partial x} = -\frac{\partial p}{\partial x} + \frac{\partial \overline{u'w'}}{\partial z} \tag{2.7}$$

In an analytical model of flow in the limit of a tall canopy on a low hill of Finnigan and Belcher (2000) and Finnigan and Belcher (2002) the momentrum balance in the upper canopy is parametrized by:

$$0 = -\frac{\partial p}{\partial x} + \frac{\partial \overline{u'w'}}{\partial z} - Ca\bar{u}|\bar{u}| \qquad (2.8)$$

where C stands for the drag coefficient of individual canopy elements and a is the leaf area per unit volume. Deeper in the canopy the shear stress gradient becomes weaker and in the lower canopy the flow reduces to a balance between the pressure gradient and the drag:

$$0 = -\frac{\partial p}{\partial x} - Ca\bar{u}|\bar{u}| \qquad (2.9)$$

As the length scale of the pressure gradient is much larger than the adjustment length scale of the canopy ($1/Ca$), the horizontal pressure gradient can be taken as constant with z through the shear stress layer and the canopy.

The most important consequences resulting from modifications of the flow by the canopy on the one hand and the hill on the other hand are summarised in the following:

- There is an increase in drag even on low hills covered with tall canopies.

- Within the canopy velocity perturbations are roughly in phase with (minus) the streamwise pressure gradient whereas those just above the canopy follow the (minus) pressure.

- Therefore velocities within the canopy peak upwind of the hill crest (Fig. 2.5) and are declining by the hill top. The difference between the in-canopy and outer layer wind velocity is largest at the hill top. The difference is at minimum half way up the hill: here the lower canopy velocity reaches its maximum and the outer layer flow has not yet increased much. This effect has strong consequences as the inflection point at the top of the canopy disappears.

- Behind the crest the mean flow is maintained by turbulent transport of momentum. In the canopy however momentum is absorbed. Only the pressure perturbation passes through the canopy and decelerates the flow. If the canopy is deep enough flow reversal may therefore be observed near the ground.

katabatic flow and wave generation: katabatic winds are formed by cooled air flowing down the mountain slopes. Radiative cooling of sloping surfaces causes the adjacent air to cool more than the free air at the same elevation. This results in a pressure gradient which in turn leads to a downslope flow. Many observations of nocturnal drainage flows have indicated that surges or fluctuations are characteristic of katabatic winds. The periods of reported oscillations range from 10-20 min (Porch et al., 1991; Coulter et al., 1989; Stone and Hoard, 1989) to 90 min (Doran and Horst, 1981). While the basic mechanism for katabatic winds is fairly well understood, the reason for the oscillations is not fully clear. They are mainly explained by the theory of compressional warming by Fleagle (1950) or by modulations of the flow by gravity waves (Gryning et al., 1985; Stone and Hoard, 1989).

theory of compressional warming: according to Fleagle the fluctuations in the flow

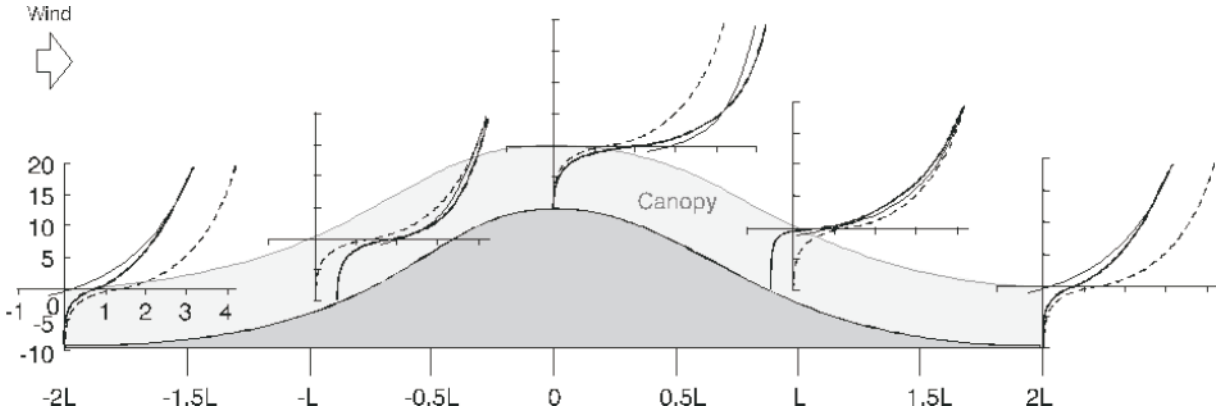

Fig. 2.5: Comparison of total velocity $u+\Delta u$ (where Δu is the perturbation velocity) in the canopy (solid line), with the no-canopy solution of the model (dashed line). The background velocity (valid only to $z=-d+z_0$) U is shown as a dotted line (from Finnigan and Belcher, 2002).

may be attributed to the accelerating and divergent downslope flow of air which weakens the initial pressure gradient. As mentioned before, an air parcel that is cooled near the surface moves downslope. However, as it moves downslope, compressional warming reduces the temperature deficit, adiabatic heating then exceeds the radiational cooling and results in a reversal of the pressure gradient. As the air decelerates, friction decreases, and radiational cooling increases the pressure gradient. The cycle then is repeated.

gravity waves: if the atmosphere is stably stratified essentially every vertical displacement of the flow leads to the generation of gravity waves. Therefore almost all terrain features generate waves. The amplitudes of terrain generated waves are proportional to the amplitude of the wave-generating terrain and therefore the spectrum of these waves is very broad. Large topographic features such as mountains and ridges can create waves that transport energy and mean-flow horizontal momentum away from the boundary layer and the lower atmosphere towards the upper atmosphere where energy and momentum become an essential component of the global circulation (Nappo, 2002). Terrain generated waves are stationary relative to the ground surface. They are thus propagating upwind at the speed of the background wind, where the background wind is the component oriented perpendicular to the mountain range or ridge.

2.2 Spectral Analysis

It is of interest to know which scales of motion contribute most to exchange processes in the atmosphere. For example we might like to know on which scales we have wave activity and if it is possible to separate it from the mean flow and / or from turbulence. As the spectrum is a measure of the frequency or scale dependent contribution to the total (co-)variance of variables this information is most conveniently addressed by spectral analysis.

Spectral analysis can be carried out by Fourier or wavelet decomposition of time series. The main advantages of wavelet decomposition lie in the localisation in both, time and frequency domain, whereas Fourier decompositions are restricted to frequency localisation. Furthermore, wavelets are much smoother (i.e. have a better resolution) in low frequencies. Their main disadvantage lies in high computational requirements.

It is not the intention to give a complete introduction in Fourier and wavelet analysis in the following sections. But the idea of representing data in frequency space and especially what information is easier accessible in this representation will be given in the following sections.

2.2.1 Energy Spectra

The following description of one- and three- dimensional spectra mainly bases on the monographs of Lumley and Panofsky (1964), Kaimal and Finnigan (1994), Sorbjan (1989) and on the paper of Biltoft (2001).

Together with Taylor's frozen turbulence hypothesis - which allows conversion of spatial scales (wavenumber) to frequency space - spectral analysis is a very suitable tool for deriving information on how energy is transferred from larger to smaller scale eddies. The value of a spectrum at a given frequency corresponds to the mean energy in that wave or at this eddy size.

Basing on an idea of Richardson, Kolmogorov (1941, 1962) postulated that scales of production and dissipation of turbulent energy are separated by the inertial subrange where energy is transferred from larger to smaller scales without any gain or loss of energy. Production of energy by buoyancy and shear 'feed' large eddies. In the inertial subrange energy cascades to progressively smaller scales until, in the dissipation range, energy is dissipated into heat by molecular viscosity.

In the inertial subrange there is a randomisation of the flow: energy tends to be distributed equally between the velocity components and correlations between velocity components are lost. The flow is locally isotropic (where local refers to wavenumber space). The transfer of energy in the inertial subrange is controlled by ε, the turbulent energy dissipation rate.

These hypotheses have led to the following model for inertial subrange turbulence:

- The three-dimensional velocity spectrum $E(\kappa)$ is a function of ε and wavenumber κ. Dimensional analysis leads to

$$E(\kappa) = \alpha \varepsilon^{2/3} \kappa^{-5/3} \tag{2.10}$$

where α is the Kolmogorov constant with a value that is estimated between 0.5 and 0.6.

- If local isotropy exists, the lateral (F_{22}, F_{33}) and longitudinal(F_{11}) one-dimensional velocity spectra are related by

$$F_{22}(\kappa_1) = F_{33}(\kappa_1) = \frac{4}{3} F_{11}(\kappa_1) \tag{2.11}$$

where κ_1 stands for the wavenumber in streamwise direction.

- By applying Taylor's hypothesis the one-dimensional wavenumber spectrum is converted to the (measured) temporal spectrum by

$$F_{ii}(\kappa_1) = \bar{u} F_{ii}(\omega). \tag{2.12}$$

The Kolmogorov hypothesis accounts for an important mechanism operating in the atmosphere, namely the energy cascade. It does however not account for effects such as e.g. wake production, where energy is extracted from large scale eddies and converted directly to energy at the smaller wake scale.

2.2.1 Fourier decomposition

The Fourier theorem states that any time series can be made of by the superposition of a series of sine and cosine waves with appropriate amplitude and phase. Figure 2.6 shows exemplarily how a square wave can be approximated by a Fourier series expansion. As more terms are added the approximation gets better.

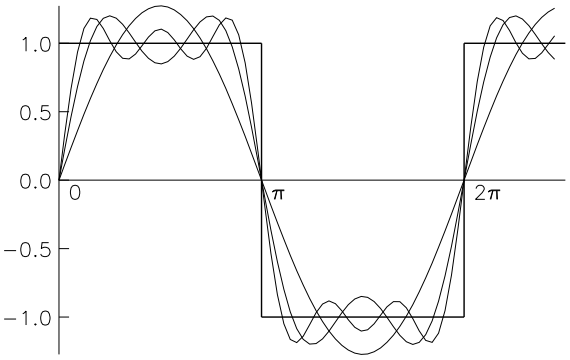

Fig. 2.6: Illustration of the harmonic synthesis of a square wave.

The Fourier transform uses this concept to convert between time and frequency domain. These are two different but equivalent descriptions of the physical system. For a continuous function of a variable *F(t)*, the Fourier transform is defined as

$$\hat{F}(\omega) = \int_{-\infty}^{\infty} F(t) e^{i\omega t}\, dt \qquad (2.13)$$

with ω standing for the angular frequency. The inverse transform reads

$$F(t) = \frac{1}{2\pi} \int_{-\infty}^{\infty} \hat{F}(\omega) e^{-i\omega t}\, d\omega \qquad (2.14)$$

where

$$e^{i\omega t} = \cos(\omega t) + i \sin(\omega t). \qquad (2.15)$$

For stationary processes the spectral energy density $S_i(f)df$ corresponds to the total variance of the Fourier transformed time series:

$$\sigma_i^2 = \int_0^{\infty} F_i(\kappa_1) d\kappa_1 = \int_0^{\infty} S_i(f)\, df \qquad (2.16)$$

where f is the cyclic frequency and related to κ by $\kappa_1 = 2\pi f / \bar{u}$.

2.2.2 Wavelet decomposition

Wavelet analysis is similar to Fourier analysis, in that time series are decomposed to certain functions. While the Fourier transform decomposes the time series into a series of sine waves ('big waves') of different frequencies, the wavelet transform uses wavelets ('small waves') instead of sine waves. Basically a small wave grows and decays in a finite time period (Fig.2.7). To be admissible a wavelet ψ must be a function that has zero mean and is localised in time as well as in the frequency domain (e.g. Daubechies, 1992). The admissibility parameter C_ψ for a wavelet function reads:

$$C_\psi \equiv 2\pi \int_{-\infty}^{\infty} \frac{|\hat{\psi}(\omega)|^2}{\omega} d\omega,\ 0 < C_\psi < \infty \qquad (2.17)$$

In essence the wavelet transform allows localisation in both time and frequency domain due to translations (τ) and dilations (λ) of the

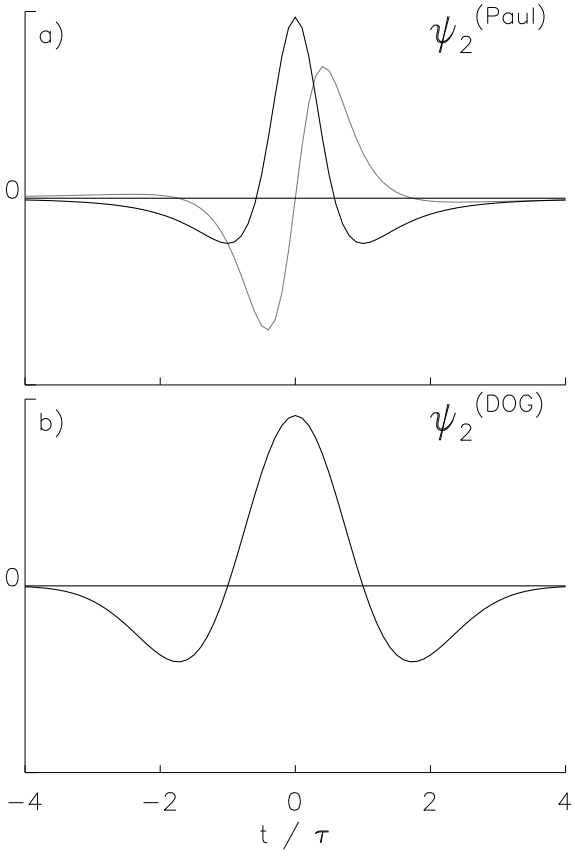

Fig. 2.7: Example of two wavelets: a) Paul wavelet of order 2 and b) the Mexican hat wavelet, which is related to the second derivative of the Gaussian probability density function. Black lines indicate the real part of the wavelets, grey lines the imaginary part.

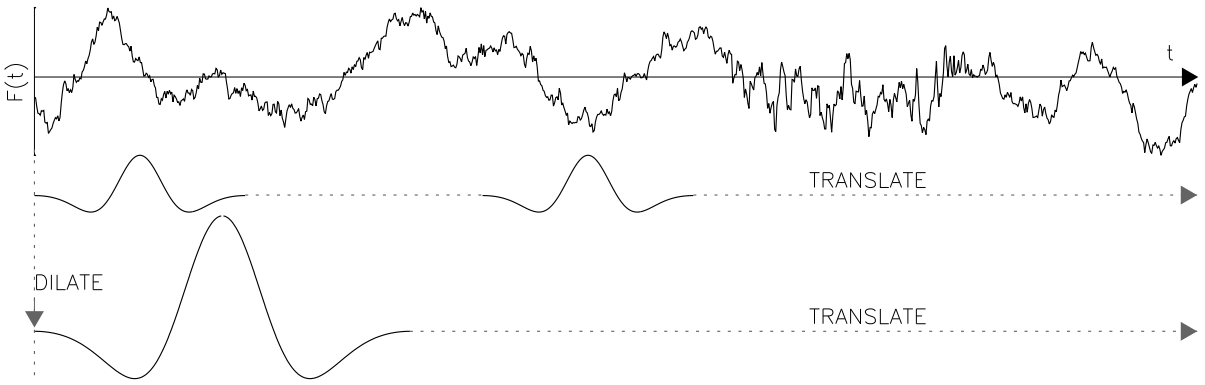

Fig. 2.8: Schematic of the dilation and translation process in a wavelet transform.

mother wavelet ψ in the scale / frequency domain (Fig 2.8). For Discrete Wavelet Transform (DWT) the dilation and translation process is based on powers of 2. For Continuous Wavelet Transform (CWT) - which uses data sampled in discrete time intervals too- the shifting process is smooth along the length of the data array.

Wavelet coefficients are calculated by

$$W(\lambda,\tau) = \int_{-\infty}^{\infty} \psi_{\lambda,\tau}(t) F(t)\, dt \qquad (2.18)$$

where

$$\psi_{\lambda,\tau}(t) \equiv \frac{1}{\sqrt{\lambda}} \psi\left(\frac{t-\tau}{\lambda}\right) \qquad (2.19)$$

$W(\lambda,\tau)$ thus represents the correlation between the wavelet $\psi_{\lambda,\tau}$ and a section of the signal.

As there is no loss of information when converting a time series with a CWT it is possible to recover the original signal from (2.18) if

$$\int_{-\infty}^{\infty} F^2(t) < \infty$$

and if the admissibility condition is fulfilled:

$$F(t) = \frac{1}{C_\psi} \int_0^{\infty} \left[\int_{-\infty}^{\infty} W(\lambda,t) \frac{1}{\sqrt{\lambda}} \psi\left(\frac{\tau-t}{\lambda}\right) dt \right] \frac{d\lambda}{\lambda^2} \qquad (2.20)$$

Moreover

$$\int_{-\infty}^{\infty} F^2(t) dt = \frac{1}{C_\psi} \int_0^{\infty} \left[\int_{-\infty}^{\infty} W^2(\lambda,\tau)\, d\tau \right] \frac{d\lambda}{\lambda^2} \qquad (2.21)$$

which means, that as the left hand side of equation (2.21) defines the energy of the signal, $W^2(\lambda,\tau) / \lambda^2$ can essentially be interpreted as an energy density function that decomposes the energy across different scales[1] and times (Percival and Walden, 2000).

types of spectra: as shown above wavelet and Fourier transforms are energy preserving:

$$E_f = \int_{-\infty}^{\infty} |f(t)|^2 dt = \frac{1}{C_\psi} \int_0^{\infty} \frac{d\lambda}{\lambda} \int_{-\infty}^{\infty} |W(\lambda,\tau)|^2 d\tau \qquad (2.22)$$

The wavelet variance is defined as

$$E_w(\lambda) = \int_{-\infty}^{\infty} |W(\lambda,\tau)|^2 d\tau \qquad (2.23)$$

For the following E_a is defined as the spectral energy of variable a in order to keep the discussion general. Fourier or wavelet coefficients are denoted by c. c can generally be divided into a real part $\Re(c)$ and an imaginary part $\Im(c)$. It has to be noted however that only for complex wavelets the imaginary part is nonzero.

The power spectrum then reads:

1 **Wavelet scale and Fourier period:** wavelets scale and Fourier period are not necessarily identical. The difference is a result of the functional form of each wavelet function. For all wavelets however there is a one-to-one relationship between wavelet scale and Fourier period which can be derived by first finding the wavelet transform of a pure cosine wave with a known Fourier period, and then computing the scale at which the wavelet power spectrum reaches its maximum. For smoothly oscillating wavelets the Fourier period is well defined (Torrence, C. and Compo, G.P.: 1998, 'A Practical Guide to Wavelet Analysis', *Bull.Am.Met.Soc.* **79**(1), 61-78.).

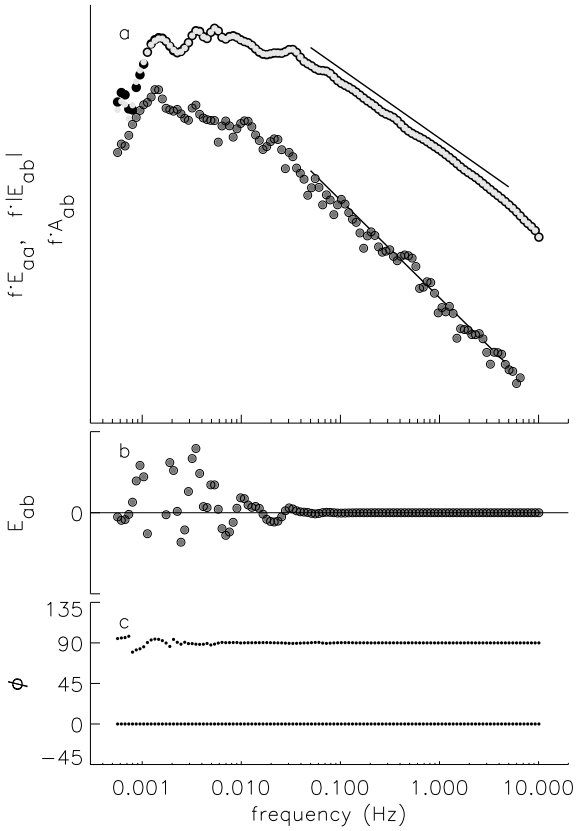

Fig. 2.9: a) black dots show an example of a log log plot of the power spectrum E_a of a variable a (data are an arbitrarily chosen run of longitudinal velocity). Variable b is identical to variable a but is phase shifted by 90 degrees with a Hilbert transform. The dark grey dots show absolute values of the cospectrum $|E_{ab}|$ between variable a and b and the light grey dots the amplitude spectrum E_{ab}, which has to be identical to the power spectrum for this artificially constructed dataset.
b) zero mean cospectrum E_{ab} between variable a and b.
c) phase spectrum between variables a and a (which of course is zero) and phase spectrum between variables a and b, which is about 90 degrees.

$$E_a = |c_a|^2 = c_a \cdot c_a{}^* = \Re(c_a)^2 + \Im(c_a)^2 \quad (2.24)$$

where * denotes the complex conjugate. More generally we have

$$\begin{aligned} E_{ab} &= \Re(c_a \cdot c_b{}^*) \\ &= \Re\left[\left(\Re(c_a) + \Im(c_a)\cdot i\right)\cdot\left(\Re(c_b) - \Im(c_b)\cdot i\right)\right] \\ &= \Re(c_a)\cdot\Re(c_b) + \Im(c_a)\cdot\Im(c_b) \end{aligned} \quad (2.25)$$

which is the same as (2.24) if $a = b$ or can be interpreted as a covariance spectrum (usually referred to as cospectrum) otherwise. The phase spectrum of two variables can be calculated as

$$\tan\phi = \frac{\Im(c_a \cdot c_b{}^*)}{\Re(c_a \cdot c_b{}^*)} \quad (2.26)$$

The algebraic sign of the resulting angle contains the information on which variable is leading. While for many applications this is of interest, we may want to discard this information when dealing with nearly isotropic turbulence. Here angles switch between -90° and 90° summing up to an angle close to 0°.

The amplitude spectrum is defined as

$$A_{ab} = |c_a \cdot c_b{}^*| = |c_a||c_b| \quad (2.27)$$

Amplitude spectra have the interesting property that, by discarding the phase, we get information about a 'potential covariance', or in other words the cospectral power that would be reached if there was no phase shift between the variables (Fig. 2.9). This is especially interesting in the inertial subrange. As the energy becomes equally distributed among velocity components we expect the amplitude spectrum to have a –5/3 dependence on the wavenumber. If there is indeed a decorrelation of the velocity components the phase must go towards 90°. Dimensional arguments (Wyngaard and Cote, 1972) have shown, that the cospectrum has a dependence of –7/3 on κ. This has been confirmed empirically.

3. Site, measurements and data handling

3.1 Site and measurements

Measurements were carried out in the Riviera valley, a section of the Ticino valley. The Ticino valley is located between the Central Alps and the Lago Maggiore area and the Riviera valley is situated between the towns of Biasca and Bellinzona (Fig 3.1). It is oriented roughly NNW-SSE and ranges from about 250 m a.s.l at the valley floor to 2500 m a.s.l on both sides. The valley is 1.5 km wide at the valley floor and eastern and western slopes are inclined at angles of 30° and 35° respectively.

Mainly on the valley floor and the westward exposed slope of the mountain range during the MAP-RIVIERA project a number of permanent sites were installed. They operated from July until mid October 1999. On most of them turbulence was measured. Furthermore additional measurements from radio sondings, tethered balloons, sodars and from a temperature profiler were carried out mainly during intensive observation periods. A detailed description of the measurements is given in Rotach et al. (2002). In the following a description of the measurements used for analysis in this thesis will be given. Measurements from the two towers used were carried out on a meadow (station E1; 46°16'00''N, 9°02'14''E, 1060 m a.s.l.) and, in a horizontal distance of roughly 500 m, in and above a mixed forest (station E2; 46°16'14''N, 9°02'11''E, 1030 m a.s.l).

At station E1 a 12 m mast was mounted close to an approximately 5 m high rock wall on a grass field in the western part of *Roasco* (Fig. 3.2). Turbulence measurements were carried out on two levels. A Metek USA1 was installed 1.5 m above ground. On top a Gill R2 was mounted at a 1.2 m boom together with a Krypton hygrometer (Table 1). Sampling intervals were 0.1 s (Metek) and 0.05 s (Gill R2 and Krypton). Raw data were stored via serial ports on a pc.

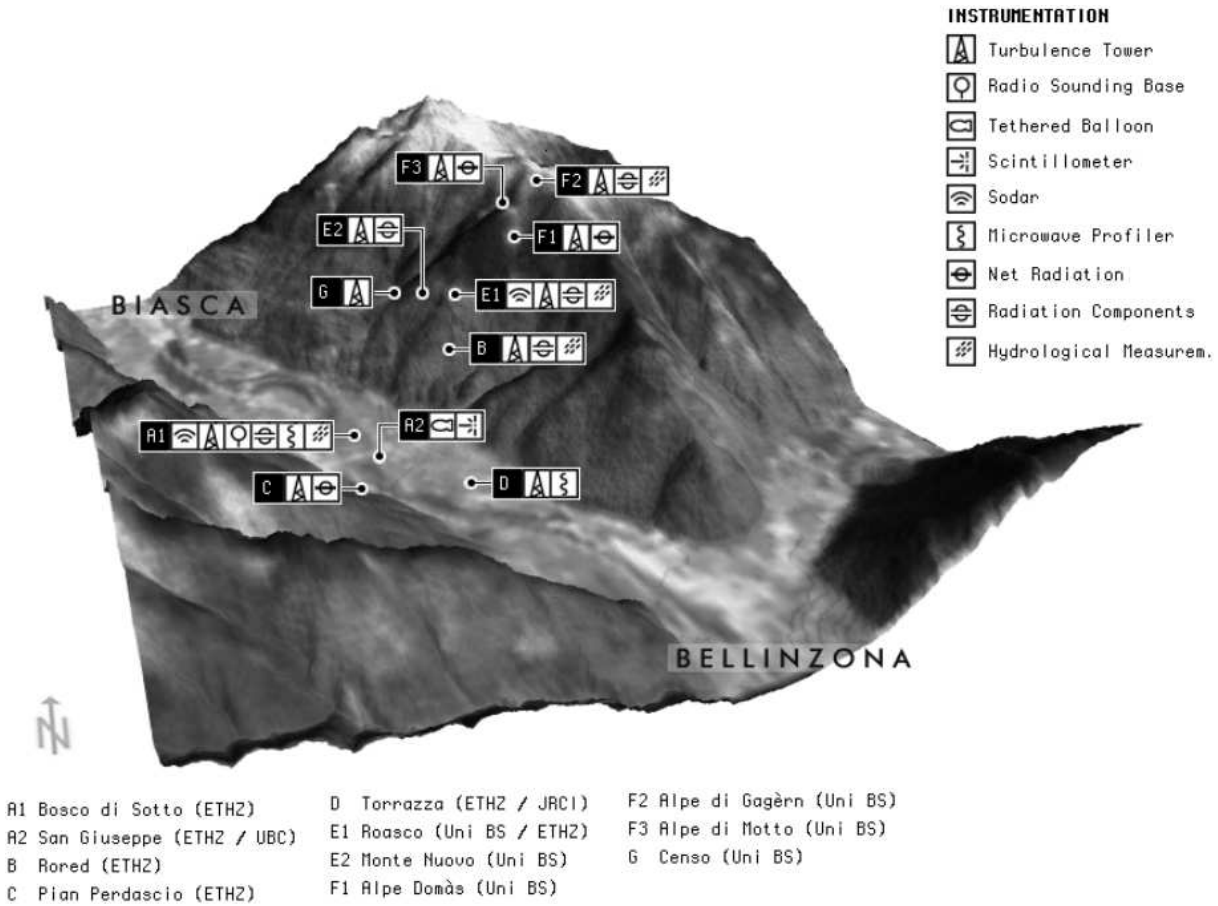

Fig. 3.1: Topographical map based on the digital elevation model of the Riviera valley (Figure by A. Christen, MCR Lab).

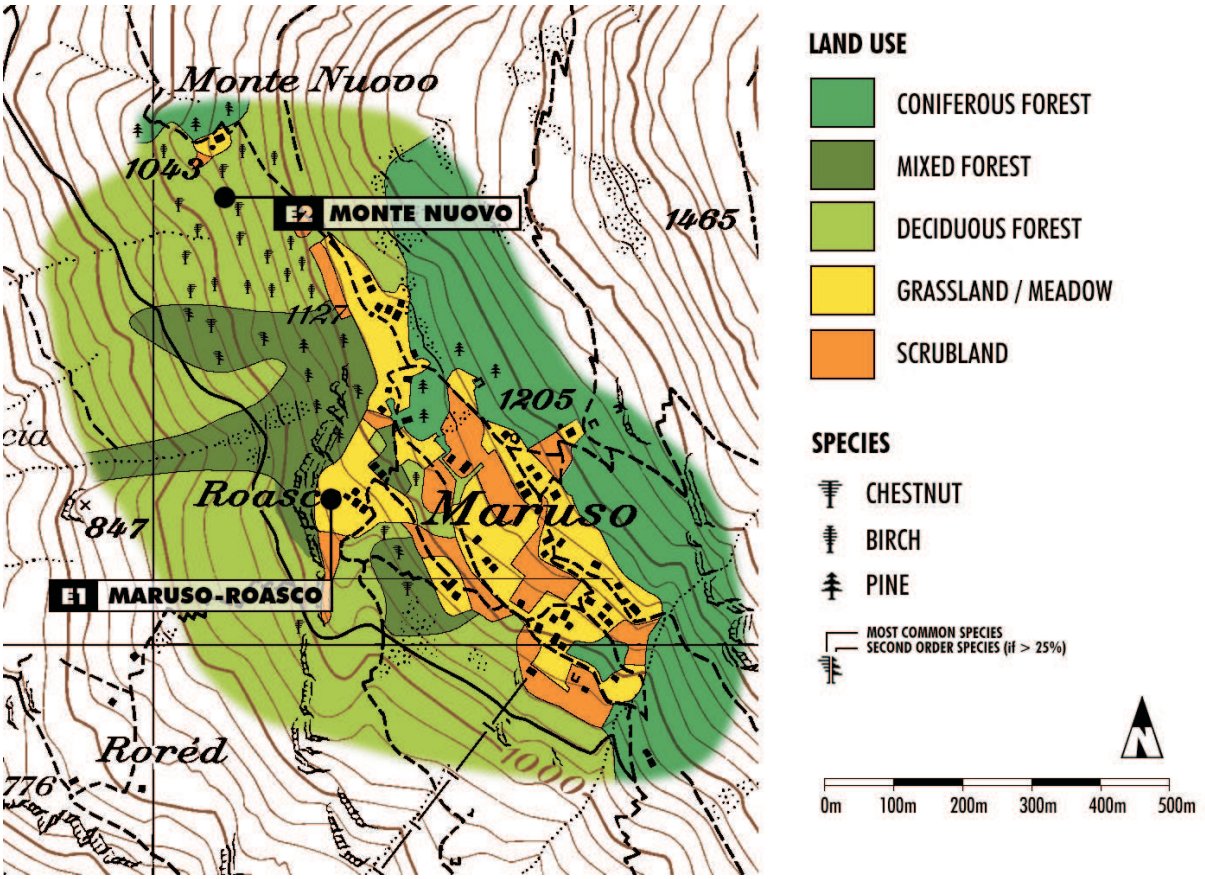

Fig. 3.2: Land use map of surrounding of tower. Base Map: Carta Nazionale della Svizzera 1314 1:25'000, 1998, © Bundesamt für Landestopographie 2000 (JD002102). (Figure by A. Christen, MCR Lab)

From Figure 3.2 it is obvious, that the mast is in a rather heterogeneous surrounding. Inclination and vegetation varied: westward, downhill, the forest bordered on a rock wall. Eastward, uphill, the slope was only 15° and after about 50 m of grassland the slope (now 35°) was covered with forest again.

At station E2 the slope was inclined by 35° and exposed to the WSW. The forest mainly consisted of birch trees, other species being chestnut, beech and hazel. The mean tree height h was 13 m and the leaf area index about 4. The forest floor was covered with sparse understorey vegetation with heights up to 0.4 m. The tower was mounted in the middle of a relatively 'homogeneous' part of the slope. Uphill and downhill, the fetch was around 150 to 200 m with similar homogeneous surface conditions, both in terms of tree height and species, prevailing 100 m slope parallel northwards and southwards (Fig. 3.2).

At the top of the 22 m high tower all components of the radiation balance were measured with a CNR1 of Kipp & Zonen. The pyrradiometer was installed slope parallel. Furthermore the mast supported, amongst others, a profile of six ultrasonic anemometer thermometers (sonics). Table 3.1 gives an overview on sonic types and measurements. Figure 3.3 shows a schematic of the tower. In order to minimise flow distortion effects the sonics where mounted slope parallel in 2 m distance from the triangular lattice tower (0.6 m side length). All raw data were stored synchronously on an industrial pc for further analysis.

Preceding the MAP-RIVIERA experiment a wind tunnel study was carried out in order to test instrument responses for several angles of attack of the flow and to create a calibration matrix for the sonics (Vogt, 1995). A subsequent field intercomparison of the sonics took place under fairly ideal conditions in order to test calibrations under 'real flow conditions' and to get information about differences between the sensors and sensor types (Christen et al., 2000).

Tab. 3.1: Overview of sonic types and measurements. The output variables *u, v, w* represent the wind velocity *components and* θ_{sv} the sonic temperature; z is the measuring and *h* the canopy height.

Notation	z(m) / z/h	Instrument type	Internal sampling rate (Hz)	Output sampling rate (Hz)	Output variables	Calibration
E2	1.74	Gill HS [1]	100.0	20.00	u,v,w,θ_{sv}	matrix
E2	1.29	Gill R2 [1]	166.6	20.83	transit counts	matrix
E2 upper canopy	0.99	Gill R2 [1]	166.6	20.83	transit counts	Gill*
E2 upper canopy	0.72	Gill R2 [1]	166.6	20.83	transit counts	Gill*
E2 upper trunk space	0.49	CSAT [2]	60.0	20.00	u,v,w,θ_{sv}	matrix
E2 lower trunk space	0.14	CSAT [2]	60.0	20.00	u,v,w,θ_{sv}	matrix
E1 top	12.7	Gill R2 [1]	166.6	20.83	u,v,w,θ_{sv}	matrix
E1 bot	2.00	Metek USA-1 [3]	10.0	10.00	u,v,w,θ_{sv}	matrix

1 Gill Instruments Ltd UK

2 Campbell Scientific Inc. USA

3 Metek GmbH, Germany

* no matrix available

Radio sondes were launched from the valley floor (site A1). The receiving system was a Vaisala MW11, the sondes were type RS80. These sondes have standard PTU sensors and a 8-channel digital GPS-receiver. The accuracy of the raw data is given by the manufacturer with 0.5 hPa, 0.2 K, 3% for the relative humidity and 0.5 m s^{-1} for wind velocity. The system is designed for a vertical range of over 20 km. As already mentioned a passive microwave temperature profiler (MTP5, Kipp & Zonen) was operated during intensive observation periods. The data analysed in this thesis were recorded at site D. The MTP5 measures the temperature from the ground to up to 600 m at a vertical resolution of 50 m and a time resolution of 5 min.

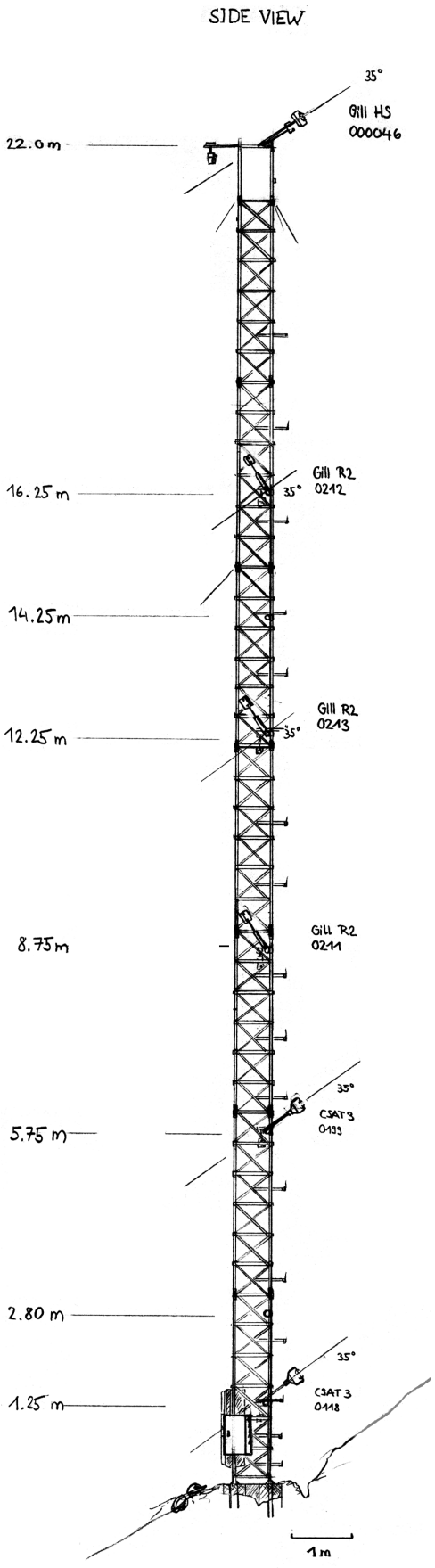

Fig. 3.3: Side view sketch of tower E2 at *Monte Nuovo* (Figure by A. Christen, MCR Lab).

3.2 Data handling

Data analysis is based on 30-min periods. For each time period and each height data are rotated into a right-handed Cartesian coordinate system with the x-axis aligned to the mean wind ($\overline{u}$) such that the mean lateral and vertical wind velocity components ($\overline{v}$, $\overline{w}$) are zero. Averages and higher order moments are calculated by applying Reynolds averaging and linear detrending (Rannik and Vesala, 1999). For some analysis it is more appropriate to rotate the coordinate system such that the x-axis points slope upwards and the y-axis points valley upwards while $\overline{w}$ is zero. Velocity components then are denoted by $\overline{u}_s$, $\overline{v}_s$, and $\overline{w}$.

An estimate of the joint probability distribution of horizontal and vertical fluctuations normalised by their respective standard deviation (u'/σ_u, v'/σ_v, w'/σ_w) is calculated by counting the number of occurrences of pairs in the same class, where the 20 times 20 classes are spaced equally between ± 2 normalised standard deviations. The result is then divided by the total number of data points leading to a probability in the range of [0, 1]. The result indicates whether there exists any dominance of fast or slow, upward or downward movements.

Information on the size of eddies dominant in the flow can be gained in several ways. The distribution of average eddy size through the whole canopy is investigated by calculating the integral length scales $L_{u,v,w}$. They are derived from the autocorrelation function

$$L_x = \frac{\overline{u}}{\sigma_x^2} \int_0^\infty \overline{x'(t)x'(t+\xi)}d\xi \qquad (3.1)$$

where x represents any velocity component and ξ is the time lag. In practice, the integration was carried out up to the first zero crossing in the autocorrelation function (Kaimal and Finnigan, 1994). Another way to assess dominant length scales is to look at the maximum peak frequency f_{max} of power spectra. In order to avoid broadening of the spectra cosine tapering was applied to the rotated and detrended data before calculating the fast Fourier transforms. Raw spectral estimates were then averaged into 60 logarithmically spaced frequency bands. For calculating mean spectra normalised single spectra were interpolated with a cubic spline and

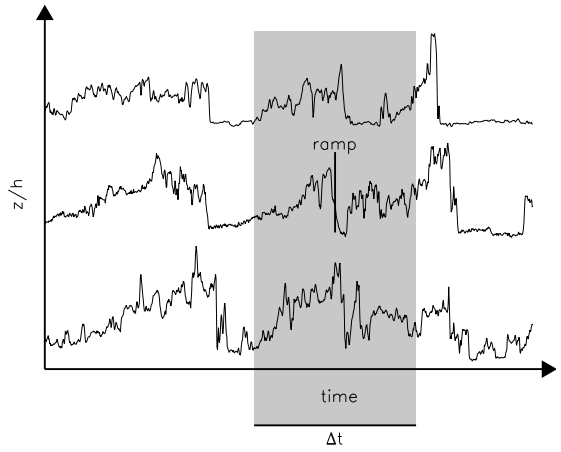

Fig. 3.4: Example of ramp pattern occurring on 3 arbitrary levels with the detection carried out on the 2nd level. The grey box indicates the time window.

the fitted curves where then averaged into logarithmically spaced classes. When calculating wavelet spectra detrending and zero padding were applied (see also section 2.2).

conditional averages and wavelet applications: practically all (geophysical) dynamics that are subject to a certain periodicity can be described and analysed with wavelet applications. Therefore there is a broad interest in this method, and applications in atmospheric research span over a wide range of timescales (e.g. Katul et al., 2001). One of the most important wavelet applications in micrometeorology, however, is the detection of organised structures, which are observed in essentially all shear flows. One can observe ramp patterns (Fig. 3.4), ejections of slowly upward moving fluid and sweeps of quickly downward moving fluid from above.

In order to investigate the importance of coherent structures in canopy flow in complex terrain a wavelet based algorithm is used for detecting these ramps (Brunet and Irvine, 2000; Feigenwinter et al., 1999; Collineau and Brunet, 1993a; Collineau and Brunet, 1993b). Knowing the time of occurrence of the ramps makes it possible to describe the dynamics of the transport processes by constructing averages of those structures and to qualitatively determine the influence they have on turbulent transport. In the following a brief description of the methodology of ramp detection and conditional averaging is given:

• The wavelet transform is carried out on 30-min data runs. Raw data are resampled to 20 Hz where necessary, linearly detrended and rotated into a streamline coordinate system.

• In order to carry out the analysis on the dominant time scale first the global wavelet spectra of vertical velocity are calculated for each run (Torrence and Compo, 1998).

• The ramp detection is carried out on the peak scale. Using a second derivative of a Gaussian (mexican hat) it is fairly easy to locate ramps as the wavelet coefficients cross zero when a steep drop in the time series is observed. Conditional averages of the time series are then sampled for all N detected events over a time window Δt

$$\langle f'(t)\rangle = \frac{1}{N}\sum_{i=1}^{N} f\left(t + t_i\right) \tag{3.2}$$

with $t_i - \Delta t/2 < t < t_i + \Delta t/2$. Δt is centered around the detection point t_i and is the mean duration of events. Angle brackets denote the conditional average.

• The mean flow during events is calculated as

$$\overline{\langle f'\rangle} = \frac{1}{\Delta t}\int_{-\Delta t/2}^{\Delta t/2} \langle f'(t)\rangle dt \tag{3.3}$$

where $\overline{\langle\ \rangle}$ denotes a time averaging operator over the detection window Δt. The mean flow calculated according to Equation 3.3 should be close to the Reynolds flux, if time windows are chosen appropriately and if coherent structures are representative of the flow.

• Measurements at canopy top are used as reference level for the detection of the events. Events have to occur coherently at all levels. A shift of ± 180 degrees is allowed, otherwise events at different levels are not considered simultaneous.

• In order to visualise different runs with slightly different dominant time scales conditional averages are binned into a time window of 1200 bins. This is done for visualisation purposes only.

4. Results

4.1 Diurnal patterns

In the following the focus is set on a period where thermally driven forcing is strong and well developed slope and valley wind systems can be expected. Therefore a period (September 7 to 15) is selected which was characterized by a flat anticyclone over North-east Europe with synoptic winds from NE that were changing to weak winds from SW to the end of the period.

Figure 4.1a shows the diurnal course of net radiation measured above the canopy. Clear sky conditions prevailed during the selected measuring period with the exception of September 11, which was slightly overcast. As stability has a crucial influence on turbulent exchange processes an overview on the distribution of stability classes is given in Fig. 4.1h. Stability is calculated by use of the Monin Obukhov length (L) which is defined as follows:

$$L = -\frac{u_*^3}{k\frac{g}{\overline{\theta}}\overline{w'\theta'_v}} \qquad (4.1)$$

and relates the production of dynamic turbulence to the production / consumption of buoyant turbulence. The production of dynamic turbulence is given by the friction velocity, which is calculated as

$$u_* = \sqrt[4]{\overline{u'w'}^2 + \overline{v'w'}^2}\,. \qquad (4.2)$$

The kinematic heat flux in (4.1) accounts for the energy exchange at the surface and the term $g/\overline{\theta}$ for buoyancy effects due to temperature variations. The von Karman constant (k) is taken as 0.4 and g is the acceleration due to gravity (9.8 m s^{-2}). The stability classes were taken from the uppermost level. In order to avoid runs measured at night with neutral to unstable stability conditions, stability classes were selected depending on a time window (see also top of Fig. 4.1h). Stability classes then are defined as follows:

$0.05 \geq h/L \geq -0.05$	neutral, evening transition
$-0.05 > h/L > -0.5$	weakly unstable, daytime
$-0.5 \geq h/L$	unstable, morning transition

Stability classes show a quite regular diurnal pattern: during daytime from around 1200 to 1800 CET a good coupling exists through the canopy. The conditions in and above the canopy are mainly unstable to weakly unstable. In the evening the atmospheric conditions typically change from neutral to weakly stable in the crown space and above, while stability conditions in the trunk space are variable. During the night stability conditions are highly variable at all levels except the lowest, where instability dominates, as well as in the lower canopy, where the regime is mainly stable. In the late morning, finally, there is a short period where unstable values can be observed in the crown space and above.

Due to the anticyclonic weather conditions a pronounced slope and valley wind system developed. Both wind systems develop due to horizontal pressure gradients that are built up hydrostatically by the changing temperature (Whiteman, 1990). The superposition of the two systems is shown in Figure 4.1b where the wind direction of two levels is depicted. One clearly sees that in the lower trunk space wind directions have almost a bimodal distribution. In the morning hours around 0900 CET the wind direction switches from downslope to upslope in connection with the changing sign of the radiation balance. In the evening the wind rotates clockwise back to a downslope direction. After having evolved the upslope and downslope winds are very persistent. This simple pattern is not found above the canopy where only in the morning transition hours upslope winds are observed for a short time. Later on in the day the upslope winds are superimposed upon an upvalley component, which becomes increasingly stronger. In the evening the wind direction often turns continuously in a counterclockwise sense to NE direction, which then shows large variability during the night.

The magnitude of wind speed $\overline{U}$ at z/h = 1.74 and 0.99 also shows a distinct pattern of temporal variation (Fig. 4.1c). During the day $\overline{U}$ decreases strongly with height but has a secondary maximum in the upper trunk space (not shown). During the night, maximum wind speed is reached at the lowest level where cold air drainage is most effective. (The diurnal patterns of the components of the wind velocity will be described in the following section in more

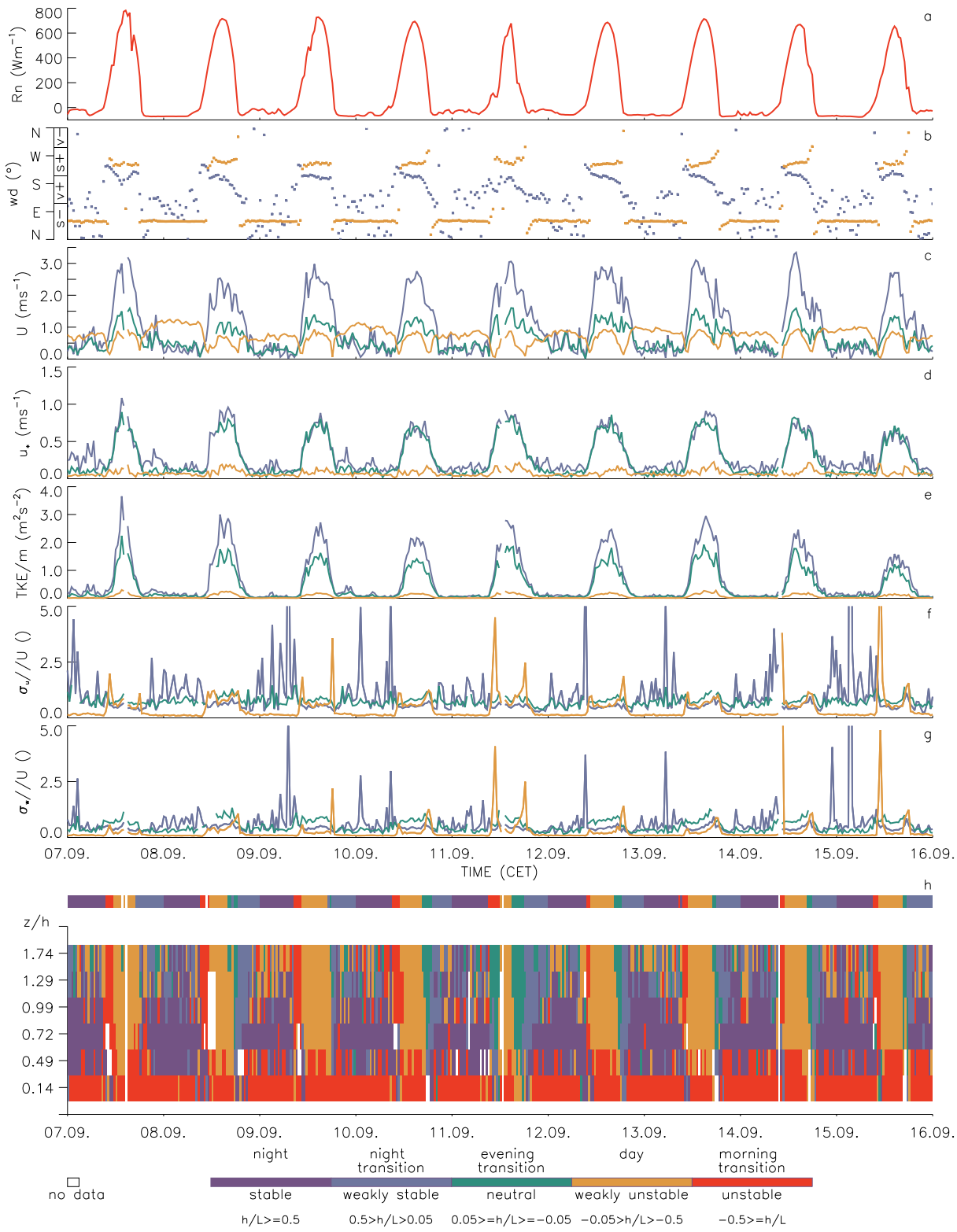

Fig. 4.1: Diurnal patterns of a) net radiation b) wind direction c) wind speed d) friction velocity e) turbulent kinetic energy per unit mass f,g) turbulence intensity of the longitudinal and vertical wind component respectively and h) the stability conditions at all measurement heights. Additionally the stability index is indicated.
Colours are used as follows: orange, green and blue lines and symbols stand for measurements at z/h = 0.14, 0.99 and 1.74 respectively. In Figure 4.1b *v* stands for valley and *s* for slope and + and – indicate upward and downward respectively.

detail.) The local friction velocity is very similar at canopy top and above but decreases rapidly in the canopy (Fig. 4.1d). Even though during the night $\overline{U}$ is strongest at z/h = 0.14, friction velocity, turbulent kinetic energy per unit mass (*TKE/m*) and the turbulence intensities are very small (Fig. 4.1e-g). This indicates a very persistent cold air drainage, which is decoupled from the flow above. Even the large changes in turbulence intensities above the canopy do not result in corresponding variations in the trunk space.

Figure 4.2a shows the mean diurnal pattern of the slope and valley wind components. At the topmost level, upslope winds are evolving when the radiation balance becomes positive. With decreasing height the switch to upslope

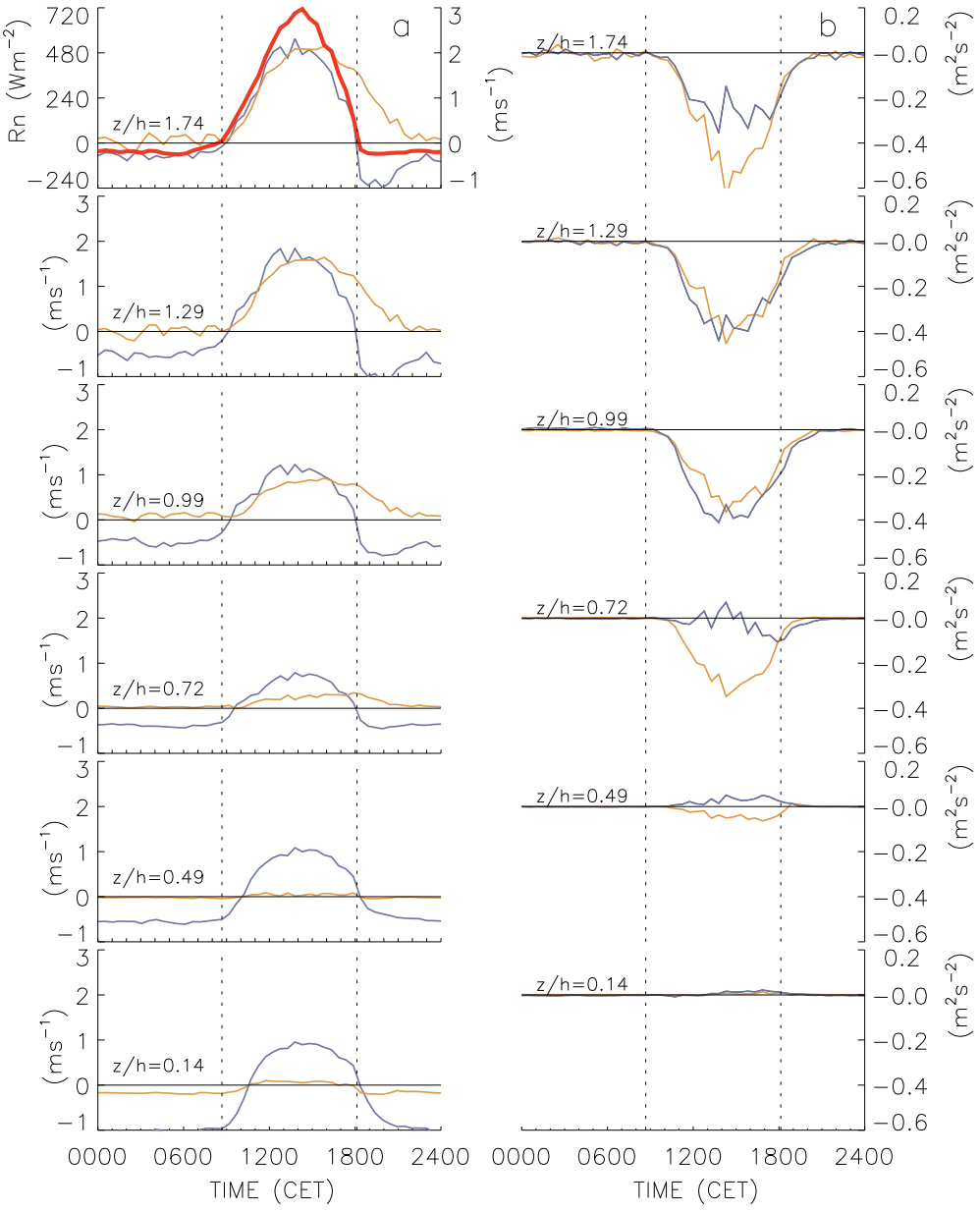

Fig. 4.2: Mean daily course from the period September 7 to 15 of a) the net radiation (thick red line in the topmost graph), the slope and the valley wind components at several values of z/h and b) $\overline{u'w'}$ and $\overline{v'w'}$ at several values of z/h. For a) positive (negative) values of blue lines indicate up-slope (down-slope) winds and positive (negative) values of orange lines stand for a velocity component along the contour line in up- (down-) valley direction. In b) blue lines stand for the longitudinal, orange lines for the lateral kinematic momentum flux. For easier orientation the changes of sign of the radiation balance are indicated as vertical dashed lines.

flow increasingly lags behind the topmost level and about 1.5 hours later upslope winds are observed at the lowest level too. In the fully developed upslope wind system a secondary maximum of wind speed is observed in the trunk space and minimum values are found in the crown space. This is contrary to the valley wind component, which decreases continuously with decreasing height and does not penetrate down into the trunk space. The valley wind system evolves with a short time lag to the slope wind system, but decays several hours later. The delay in the evening transition between the top and the lowest level for the slope component is only about half as long (40 min) as that in the morning. During the night a maximum cold air drainage flow is located in the lower trunk space. In the canopy wind speed is reduced and a secondary maximum lies just above the canopy; with further increasing height wind speed decreases.

Reynolds stress $\overline{u'w'}$ (Fig. 4.2b) is greatest just above the canopy. In the lower canopy and in the trunk space $\overline{u'w'}$ becomes very small and is mainly positive. The canopy hence acts as a sink for longitudinal momentum for the flow both above and beneath it. Another interesting feature is the lateral kinematic momentum flux $\overline{v'w'}$, which, after rotating the coordinate system into the mean wind becomes zero on an infinite flat plane and negligibly small at near ideal sites (Kaimal and Finnigan, 1994). In situations where two wind systems of different (spatial and time) scale are interacting this can of course not be expected. Directional shear causes a lateral momentum transport that is in the same order or even larger than the longitudinal one. In the trunk space where winds are essentially directed slope upwards negative daily $\overline{v'w'}$ values represent a momentum transport in the upvalley direction and $\overline{v'w'}$ decreases continuously with decreasing height. At night momentum fluxes are generally very small and of varying sign.

4.2 Turbulence characteristics in the neutral / unstable boundary layer

4.2.1 Turbulence profiles

In the 'family portrait', where common features of profiles of different canopies are depicted (e.g. Raupach, 1988), mainly neutral and near-neutral conditions are analysed. Therefore we show the neutral values of vertical profiles of turbulence statistics ±1 standard deviation for comparison. The most frequently observed class, however, is that for weakly unstable daytime conditions. Additionally, unstable values from the morning transition time are given. In the following the abbreviation CL_h is used for a canopy layer at height $z = h$ and SL stands for surface layer. Reference neutral surface layer values are taken from Panofsky and Dutton (1984) whilst canopy layer values are taken from Raupach et al. (1996) and Finnigan (2000).

The neutral $\overline{u}/\overline{u}_h$ profile in Figure 4.3a is comparable to the profiles of the family portrait. The wind profile is inflected and gradients reach maximum values at $z = h$. Standard deviations are small, indicating that a good coupling exists between different levels. There is a strong decrease of $\overline{u}/\overline{u}_h$ with descending height and minimum values are reached at the lowest level. This is not the case both for unstable and weakly unstable profiles. Even though these profiles are very similar in and above the canopy they show thermally induced wind speed maxima in the trunk space. During the morning transition the still dominating cold air drainage leads to maximum wind speeds at the lowest level and during the day buoyancy driven upslope winds lead to a maximum in the upper trunk space.

In the literature, above canopy flow is usually characterised by a constant momentum flux; within canopy $\overline{u'w'}$ decreases rapidly. Here, as already mentioned, $\overline{u'w'}$ is greatest just above the canopy during daytime conditions and becomes very small and even mainly positive in the canopy layer whereas $\overline{v'w'}$ decreases continuously with decreasing height for all stability classes (Fig 4.3b,c). More information about momentum transport mechanisms can be gained by examining the joint probability distribution of the normalised velocity fluctuations (Fig 4.4). Above the canopy the joint probability $P(u',w')$ as well as $P(v',w')$ is highest in the second quadrant. Momentum is thus most frequently transported by ejections, slower moving air masses that are transported upwards. Contributions of larger magnitude however arise from sweeps that transport faster moving air downwards. For longitudinal momentum transport this ejection sweep dominance is not as distinctive as observed over other forests (e.g. Maitani and Shaw, 1990; Shaw et al., 1983), and is thus less organised. In the trunk space and during daytime in the upper canopy interactions are most frequent, resulting in a small but upward directed $\overline{u'w'}$. Distributions of (v',w'), however, become increasingly symmetric towards the ground indicating continuously smaller fluxes with decreasing height. Generally distributions at $z/h = 0.99$ show a stronger kurtosis, especially in crown space where mainly small fluctuations of the second quadrant contribute to the flux and momentum transport is most intermittent with few large events determining the flux. For $P(u',w')$ this is consistent with observations over other rough surfaces (e.g. Kruijt et al., 2000).

Figures 4.3d-f show the normalised standard deviations of the wind components. Positive deviations of $\sigma_u / u_{*(top)}$ from surface layer scaling are often attributed to large-scale disturbances that scale with the height of the planetary boundary layer (e.g. De Bruin et al., 1993, Peltier et al., 1996). Here, however, fluctuations in the longitudinal direction are small even above the canopy compared to both, SL and CL_h values (Fig. 4.3d). As spectral analysis shows (Fig. 4.5) there are few large-scale disturbances, possibly because large-scale eddies are topographically forced to remain stationary. Normalised σ_v values reach surface layer values well above the canopy (CL_h values were not found in literature for the lateral component). Neutral $\sigma_w / u_{*(top)}$ values above the canopy are slightly higher than SL values and reach SL values at $z = h$. Weak unstable and unstable above-canopy values lay in the range that one would expect in the surface layer; all second moments decrease rapidly in the canopy, which is in agreement with the 'family portrait'.

In forests over flat terrain the correlation coefficient of the longitudinal and vertical wind velocity components r_{uw} usually increases towards the rough surface and has a value of -0.5

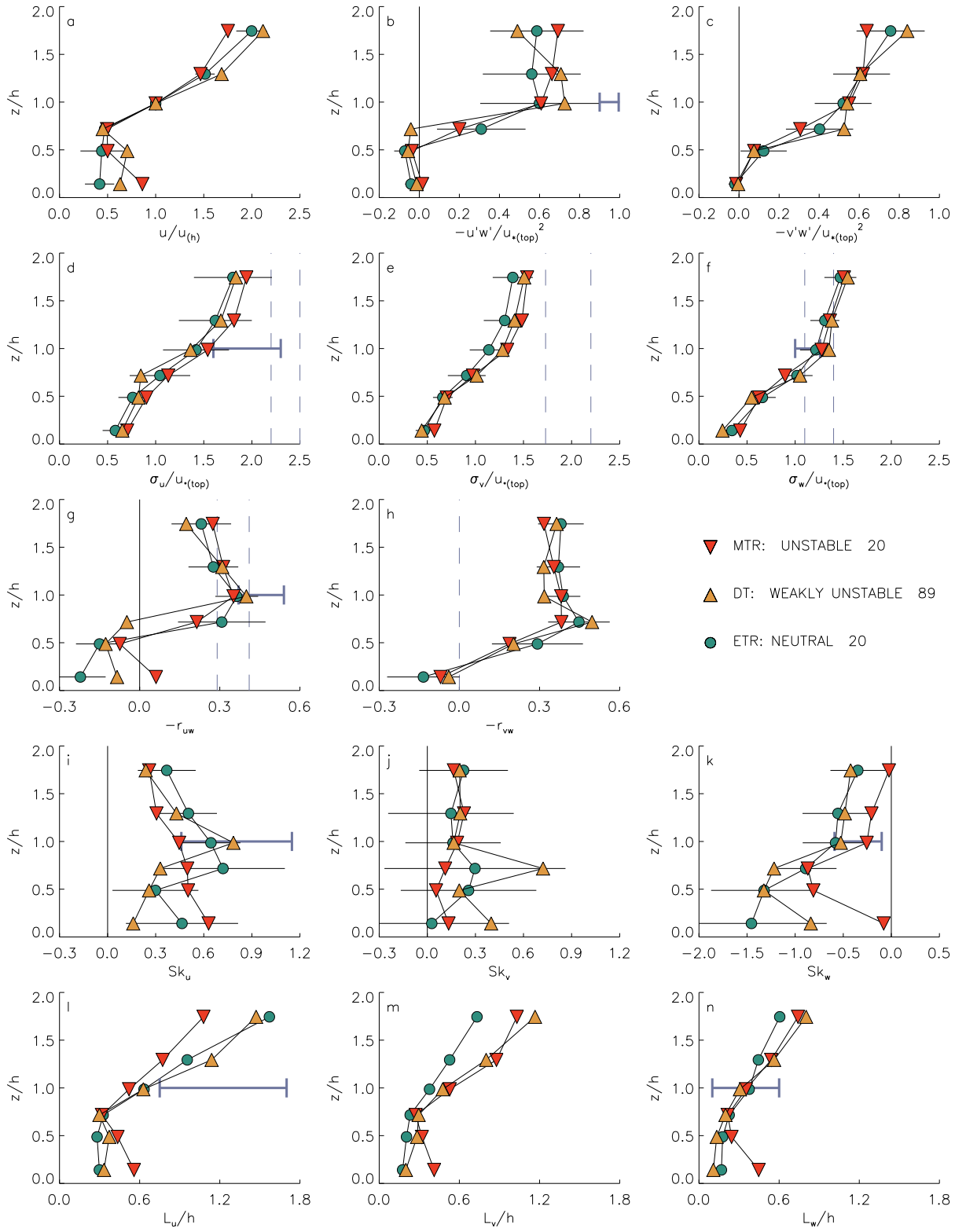

Fig. 4.3: Normalised vertical profiles of a) $\overline{u}/\overline{u}_h$ b) $-\overline{u'w'}/u^2_{*(top)}$ c) $-\overline{v'w'}/u^2_{*(top)}$ d,e,f) $\sigma_u/u_{*(top)}$, $\sigma_v/u_{*(top)}$ and $\sigma_w/u_{*(top)}$ g,h) the correlation coefficients -r_{uw} and -r_{vw} i,j,k) the skewnesses of u,v,w and l,m,n) the length scales L_u/h, L_v/h and L_w/h, respectively. Error bars (for reasons of clarity they are only given for neutral values) stand for ±1 standard deviation. Dashed blue lines indicate ranges or values observed in the neutral surface layer (Panofsky and Dutton, 1984). Canopy-layer expectation ranges (Raupach et al., 1996) are given with blue horizontal lines in $z/h = 1$. Symbols show stability conditions and number of runs used in the respective profile.

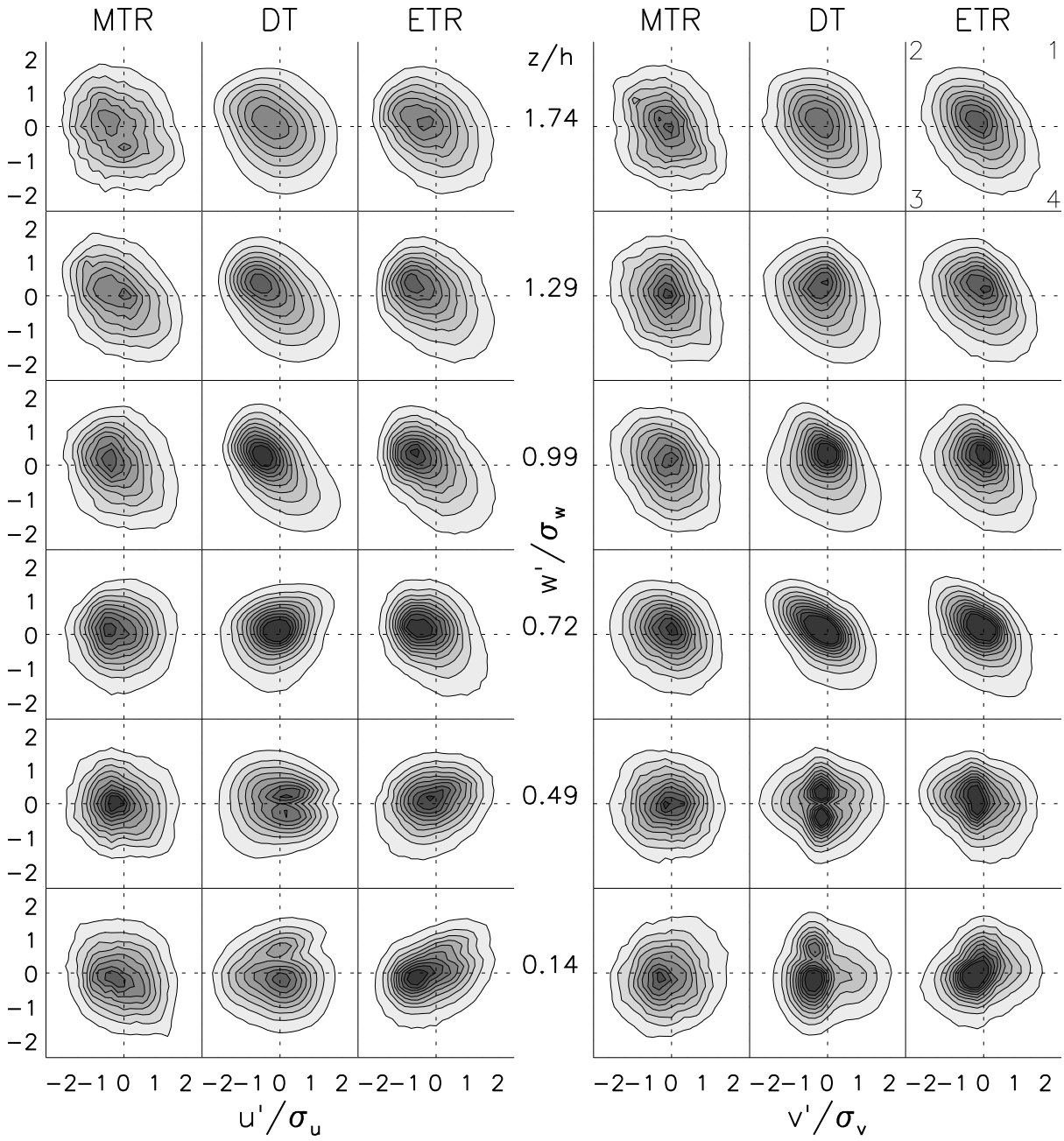

Fig. 4.4: Joint probability distributions $P(u,w)$ and $P(v,w)$ of normalised fluctuations. Contour lines stand for 0.001 probability intervals. For the outermost contour $P = 0$. Definition of quadrants is given in the graph in the upper right corner.

at CL_h. Figure 4.3g shows that r_{uw} increases towards the canopy but there only values close to those measured in a SL is observed. Contrary to both SL and CL where r_{vw} is close to zero here r_{vw} values are relatively large for all but the lowest level. In the canopy all correlation coefficients decrease quickly and reach positive values for r_{uw}. Even though longitudinal momentum transport is not as effective as observed over other rough surfaces directional shear leads to the fact that more momentum is extracted from the mean flow than in both, SL and CL.

Longitudinal skewnesses in crown space are towards the lower end compared to those observed in the family portrait (Fig. 4.3i-k). Above the canopy however skewnesses do not drop to zero as rapidly as over forests in flat terrain. The positive u,v and the negative w third-order moments indicate that ejection sweep cycles are important for momentum transport in the upper canopy as is confirmed by the joint probability density functions of the velocity fluctuations (Fig. 4.4). But smaller CL correlation coefficients and skewnesses indicate

that exchange mechanisms are less efficient and not as organised as over flat terrain.

According to Raupach et al. (1996) length scales L_u in the upper canopy are typically in the order of h. Here L_u/h is found to be towards the lower end compared to those observed in other forests (Fig. 4.3l-n) but increases quickly above the crown space. With $L_{w(h)}/h = 0.307$ $L_{w(h)}$ is around $h/3$, which coincides with literature values. Raupach et al. (1996) suggested that the basic shear length scale in a canopy flow is

$$L_s = \frac{u_h}{(\mathrm{d}u / \mathrm{d}z)_{z=h}} \tag{4.3}$$

and lies typically around $0.5h$ in moderately dense forests. From the mixing layer analogy they expected Λ_x, the x-distance between dominant eddies, to be in the range of 7 to 10 times L_s and found a mean value of 8.1 for all canopies they investigated. They further suggested that Λ_x is related to L_w by

$$\Lambda_x = 2\pi L_{w(h)} \frac{U_c}{\overline{u}_{(h)}} \tag{4.4}$$

where U_c represents the convection velocity of eddies. Here L_s was estimated from the measurements at $z/h = 0.99$ and the two neighbouring levels. For daytime conditions it lies at $0.46\ h$ and therefore very close to the values observed in other moderately dense forests. If $1.8\ \overline{u}_{(h)}$ is used as an empirical value for U_c (e.g. Shaw et al., 1995) then $\Lambda_x/h = 3.47$ and thus Λ_x is 7.6 times L_s, which is in good agreement with the mixing layer analogy too. Further information on length scales can also be obtained by the maximum peak frequency f_{max} of spectra, which will be discussed in the following chapter.

4.2.2 Spectral characteristics

Figure 4.5 shows the normalised spectra of the wind velocity components. Several studies over flat terrain (e.g. Kaimal and Finnigan, 1994) have shown, that, if the frequency axis is scaled with the mean canopy height h and the wind velocity ($\overline{u}_h$), the position of peaks does not vary with height through the roughness sublayer (RS) to the mid canopy height.

Above the canopy, in the roughness sublayer, one has observed that energy is removed from the mean flow and injected into coherent eddies. In the canopy work is done against pressure drag and against the viscous component of canopy drag. Kinetic energy is then directly converted into fine scale wake turbulence and heat (Kaimal and Finnigan, 1994). These processes extract energy from the mean flow in the energy containig range and from eddies of all scales larger than the canopy elements in the inertial subrange. This continuous removal of energy from the eddy cascade leads to a violation of the assumptions leading to Kolmogorov's hypothesis.

The positions of the spectral peaks are given in Table 1. For the vertical velocity component the peaks lie in the range of literature values and they are fairly constant with height through the crown space. Relating the spectral peak frequency in $z/h = 0.99$ with Λ_X leads to

$$\frac{\Lambda_x}{h} = \frac{U_c}{f_{\max(w)} \cdot h} \tag{4.5}$$

and results in $\Lambda_x/h = 3.76$, a value that is in good agreement with the value evaluated using the integral length scale and therefore with the mixing layer analogy too. Lateral peak frequencies that have been measured in other forests are more variable than those of the other velocity components. Here they lie in the indicated range of canopy data and they are fairly constant with height. This is not the case for the longitudinal component under weak unstable conditions. While at $z/h \geq 0.99$ the main energy contribution derives from eddies of similar size as observed in other studies, larger eddies seem to be suppressed in the crown space and peak frequencies are shifted to higher values. The reason for this is not clear. In the morning and evening transitions, however, the spectral peaks are fairly constant with height.

There are remarkably few disturbances on the low frequency side of the spectra. While longitudinal and lateral spectra usually show quite large scatter that is caused by eddies larger than SL scales (e.g. Kaimal, 1978; Peltier et al., 1996), here spectral power falls off quickly on the low frequency side of the peak even under daytime conditions. Large-scale eddies might thus be topographically forced to remain

Tab. 4.1: Scaled peak frequencies f_{max} for all velocity components and weak unstable (daytime) conditions. For comparison, literature values from Kaimal and Finnigan (1994) are indicated.

z/h	$f_{max(u)}h/\overline{u}_h$	$f_{max(v)}h/\overline{u}_h$	$f_{max(w)}h/\overline{u}_h$
Lit. values	0.15±0.05	0.10−0.35	0.45±0.05
1.74	0.14	0.23	0.37
1.29	0.17	0.25	0.46
0.99	0.21	0.27	0.48
0.72	0.53	0.20	0.46
0.49	0.30	0.19	0.43
0.14	0.18	0.19	0.55

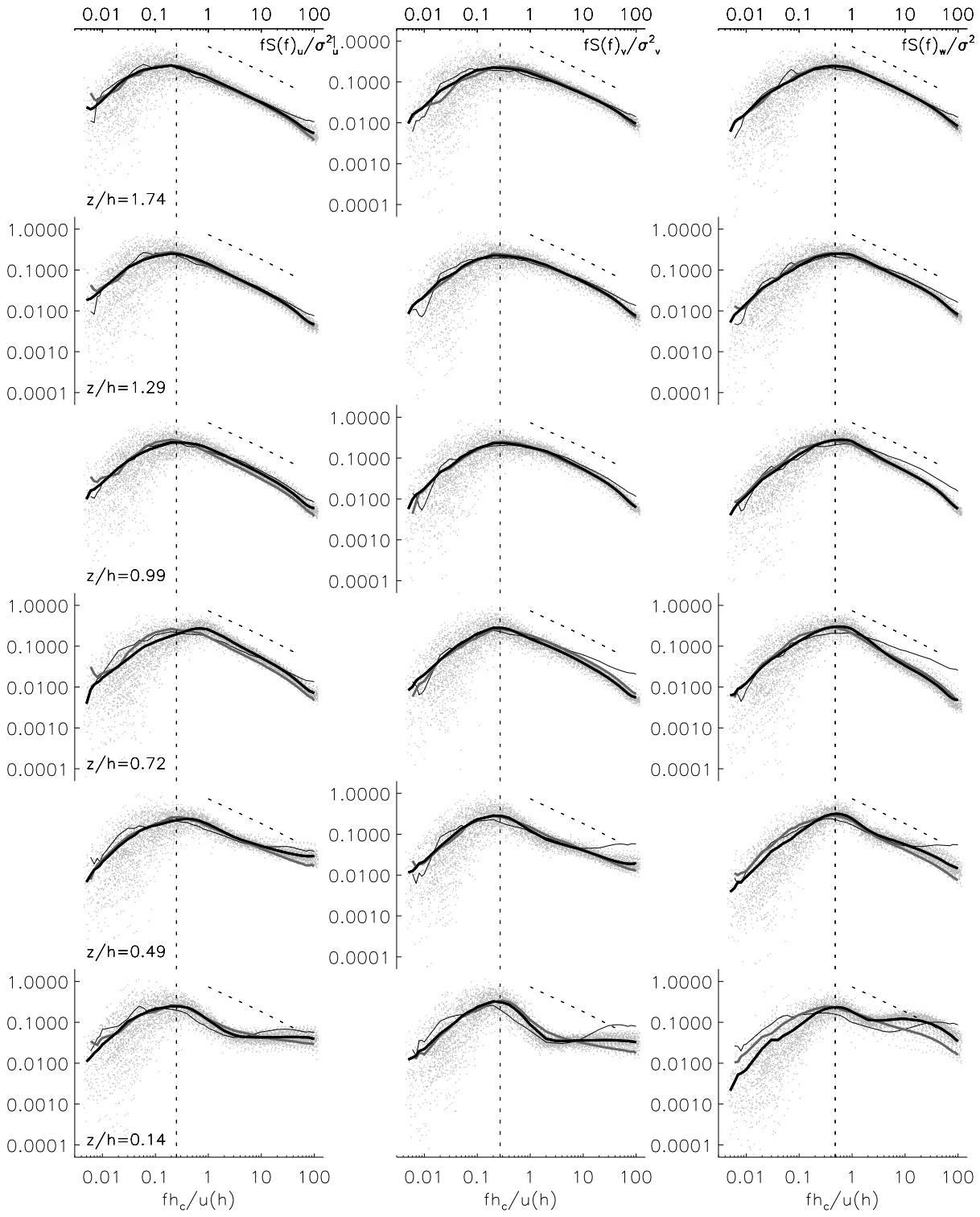

Fig. 4.5: Normalised power spectra of all velocity components. Black thick line and grey symbols indicate weakly unstable spectra. Grey thick and black thin lines stand for unstable and neutral spectra respectively. Black dashed lines indicate –2/3 slope of the inertial subrange. For easier orientation the vertical dashed line is given, indicating the peak frequency at z/h=0.99.

stationary. Apart from the daily cycle when a steady slope and valley wind system develops there is a quite sharp separation between mean flow characteristics and turbulence.

From the highest measurement level through the crown space longitudinal power spectra are 'well behaved' in the sense that they follow the expected -2/3 slope in the inertial subrange closely over roughly two decades (Tab. 4.2). Lateral power shows a smaller roll off at all measurement levels and vertical spectra have a smaller roll off above the canopy and a stronger than the -2/3 roll off from canopy top downwards. In general the canopy spectra show an increasingly strong relative power deficit in the lower inertial subrange when approaching and descending through the canopy. This is most notable for spectra of the vertical wind component and may be attributable to wake and waving production processes that extract energy of the lower intertial subrange and lead to a more pronounced importance of smallest-scale turbulence. This can be seen most clearly in the trunk space where turbulence levels are generally low. It is unlikely that aliasing is the cause of this additional energy above the Nyquist frequency as data collected with CSAT3 has been oversampled three times which reduces aliasing effects. Especially vertical spectra give reason to assume a source of smallest scale turbulence which may be attributed to wake turbulence generation (Kruijt et al., 2000; Mazzoni, 1996).

Tab. 4.2: Inertial subrange slopes for all velocity components and weak unstable conditions calculated from normalised frequencies in the range of 1 to 10 Hz.

z/h	slope$(fS_u(f))$	slope$(fS_v(f))$	slope$(fS_w(f))$
Lit. values	-2/3	-2/3	-2/3
1.74	-0.62	-0.53	-0.59
1.29	-0.64	-0.56	-0.61
0.99	-0.63	-0.58	-0.72
0.72	-0.69	-0.61	-0.89

According to Kaimal and Finnigan (1994) too few cospectra have been published for turbulence over canopies to draw any general conclusions neither on the slope nor on the position of peaks. Only indications were given that the position of the cospectral peak of longitudinal momentum follows $f_{max(u)}/\overline{u}_h$.The slope was measured to roll off as f^{-1} (Amiro, 1990; Baldocchi and Hutchison, 1987) or as standard $f^{-4/3}$ (Shaw et al., 1974). While in the meantime there have been several publications on cospectra of scalars, there still are fairly little publications on cospectral properties of momentum (e.g. Su et al., 1998).

Figure 4.6 shows characteristics of cospectra between the velocity components. It has to be noted that cospectra for single runs are ill defined in the sense that there are frequent changes in sign. In order to get information about the mean cospectral behaviour, means of the absolute values of cospectra ($|C|$) are shown. Cospectral levels may be low either as there is little turburlence or as fluctuations of the velocity components are uncorrelated. Therefore amplitude spectra (A), which may be interpreted as potential covariance, and absolute values of phase angles, ($|P|$) which are a measure for the correlation between the variables (see also section 2.2), are shown additionally.

The roll off of amplitude spectra mainly lies between the roll offs of the variables that contribute to it (Tab. 4.3). The energy in the lower inertial subrange is shifted to smaller wavelengths as is observed for power spectra

($fS_w(f)$). Generally the slopes flatten out with decreasing height.

The means of the absolute values of cospectra are less well defined than the amplitude spectra. Values given for the slope should therefore be taken as rough estimates only. The slope of the cospectra too indicates that there are processes in turbulence transport not accounted for by more idealised spectral models (e.g. Wyngaard and Cote, 1972). The roll offs of both $f|C|_{uw}$ and $f|C|_{vw}$ get faster towards the canopy and flatten with decreasing height from canopy top downwards. For $f|C|_{vw}$ the roll off increases from f^{-1} dependence above canopy to $f^{-4/3}$ in the canopy.

The peak frequencies of cospectra are better defined than the slopes (Tab 4.4). At canopy top and above $f_{\max}|C|_{(uw)}h/\bar{u}_h$ follows quite closely the peak in its according amplitude spectrum, while peak frequencies for the longitudinal power spectrum are found at lower frequencies. Towards the peak frequency of $f_{\max}|C|_{(uw)}h/\bar{u}_h$ phase spectra of longitudinal momentum show a secondary maximum. Phase spectra of lateral momentum on the other hand decrease continuously. The peak frequency $f_{\max}|C|_{(vw)}h/\bar{u}_h$ is shifted to smaller than $f_{\max}A_{vw}(f)$ values. For both, longitudinal and lateral momentum flux peak frequencies are shifted to slightly higher frequencies with decreasing height through the canopy.

Tab. 4.3: Inertial subrange slopes for $fA_{uw}(f)$, $fA_{vw}(f)$, $f|C|_{uw}(f)$ and $f|C|_{vw}(f)$ under weak unstable conditions calculated from normalised frequencies in the range [3,10].

z/h	*Slope(fA_{uw})*	*Slope(fA_{uw})*	*Slope($f\|C\|_{uw}$)*	*Slope($f\|C\|_{vw}$)*
Lit. values	-2/3	-2/3	-1 or -4/3	-1 or -4/3
1.74	-0.61	-0.56	-0.76	-0.99
1.29	-0.66	-0.58	-1.20	-1.08
0.99	-0.73	-0.64	-1.47	-1.35
0.72	-0.75	-0.77	-1.11	-1.29

Tab.4.4: Scaled peak frequencies for $A_{uw}(f)$, $A_{vw}(f)$, $|C|_{uw}(f)$ and $|C|_{vw}(f)$ under unstable (daytime) conditions. As the position of the cospectral peak of longitudinal momentum is expected to follow $f_{max(u)}/\bar{u}_h$, values of Tab.4.2 are given for comparison.

z/h	$f_{\max}(A_{uw})h/\bar{u}_h$	$f_{\max}(A_{vw})h/\bar{u}_h$	$f_{\max(u)}h/\bar{u}_h$	$f_{\max}\|C\|_{uw}\,h/\bar{u}_h$	$f_{\max(u)}h/\bar{u}_h$	$f_{\max}\|C\|_{vw}\,h/\bar{u}_h$
1.74	0.24	0.22	0.14	0.22	0.23	0.14
1.29	0.29	0.23	0.17	0.27	0.25	0.14
0.99	0.35	0.27	0.21	0.33	0.27	0.16
0.72	0.41	0.23	0.53	0.34	0.20	0.22
0.49	0.34	0.26	0.30	0.19	0.19	0.20
0.17	0.27	0.25	0.18	0.25	0.19	0.24

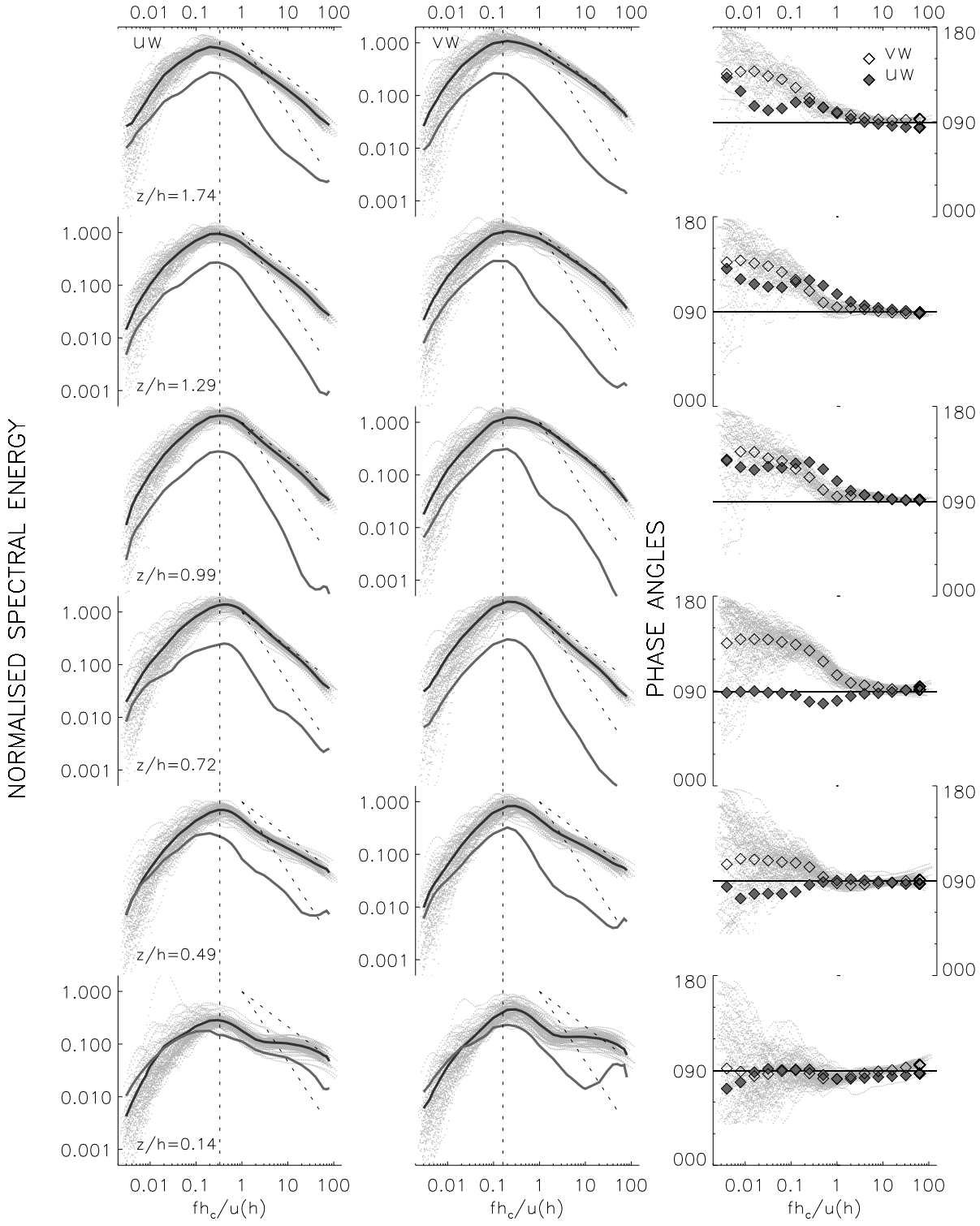

Fig. 4.6: Normalised cospectral power of longitudinal and lateral momentum fluxes. Black thick line and grey symbols indicate amplitude spectra. Grey thick lines indicate means of the absolute values of cospectra and symbols in the third column stand for phase spectra. Symbols are indicated in the first row. Black dashed lines indicate –2/3 and -4/3 slope of the inertial subrange. For easier orientation the vertical dashed line given indicates the peak frequency of cospectra at *z/h*=0.99.

From the phase spectra it can be seen that from canopy top towards both above and in canopy flow *u'* in the energy containig range is increasingly decorrelated from *w'* resulting, in accord with the turbulence profiles, to a decreasing longitudinal momentum flux. In the canopy *u'* and *w'* are essentially decorrelated. This results from pressure perturbations, as will be shown in section 4.2.3.

4.2.3 Coherent structures

Shear flows are characterised by organised, coherent patterns of ejections of slowly upward moving fluid and sweeps of quickly downward moving fluid from above (see also Section 2.1.1). These eddies are usually connected with temperature ramps; tilted microfronts that propagate in downwind direction (e.g. Raupach and Thom, 1981; Shaw and Zhang, 1992; Gao et al., 1992).

Positive u, v and negative w as well as the joint probability functions of the velocity fluctuations indicate, that ejection sweep cycles are important for turbulent transport in the canopy at station E2 (Section 4.2.1). In order to get an idea about the vertical coupling and about exchange mechanisms it is of interest to isolate such structures. For this purpose a wavelet based algorithm was applied (Section 3.2) with which it is possible to detect ramp structures (Feigenwinter, 2000 and Collineau and Brunet, 1993a+b).

The wavelet transform was carried out for 30 min data runs which were resampled to 20 Hz where necessary, detrended and rotated into a streamline coordinate system. The analysis has been carried out for weak unstable data (82 runs) of the time period from September 7 to 15 (see Sections 4.2.1 and 4.2.2). Even though temperature time series are most commonly used for the detection of coherent structures (as they usually build up microfronts that are connected to the ejection-sweep cycle), here time series of vertical velocity were used, following the argumentation of Brunet and Irvine (2000) that both temperature and streamwise velocity time series include contributions from inactive turbulence. Vertical velocity is more closely related to active turbulence that affects the vertical exchange of momentum.

Coherent structures are not a regular feature of canopy flow. More quiescent periods are alternating with periods with strong vertical mixing by these relatively large eddies that span through the whole canopy. Figure 4.7 shows the mean time interval between the structures. One can easily see that the distribution is skewed.

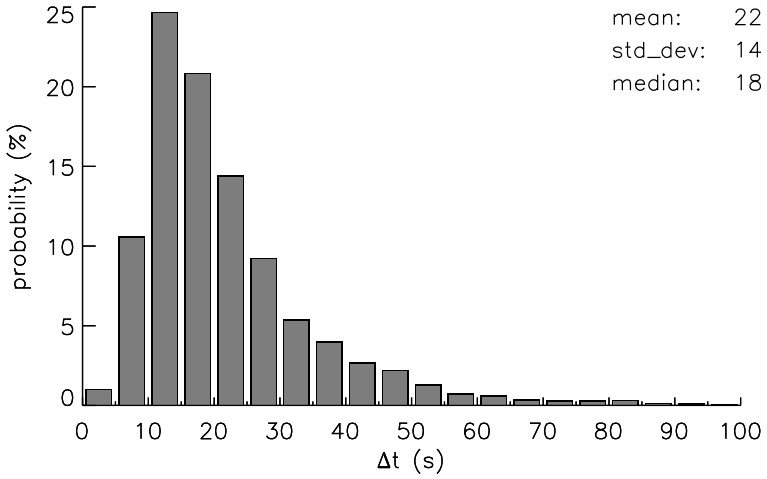

Fig. 4.7: Distribution of time interval Δt between detection of coherent structures.

The skewness in the distribution of Δt can, of course, cause problems when calculating conditional averages. However if the flow is characterised by coherent structures and if the time interval chosen is appropriate for the flow, the mean conditional average of (co-)variances (Eq. 3.3) should be close to the conventional Reynolds flux. The ratios given in Table 1 indicate that the flow is fairly well represented by the conditional averages.

In Figure 4.8 conditional averages of the coherent structures are depicted. At the reference level in z/h = 0.99 slower moving air is ejected from the canopy and then replaced by colder, faster moving air from above. Longitudinal momentum sweeps are stronger than ejections, confirming results from joint probability

Tab. 4.5: Ratios of conditional average of longitudinal and lateral momentum flux to conventionally calculated Reynolds flux.

z/h	$\frac{1}{N}\sum_N \frac{\overline{\langle u'w' \rangle}}{\overline{u'w'}}$	$\frac{1}{N}\sum_N \frac{\overline{\langle v'w' \rangle}}{\overline{v'w'}}$
1.74	1.01	1.04
1.29	1.03	1.01
0.99	1.06	1.01
0.72	1.02	1.03
0.49	1.08	0.98
0.14	0.98	0.97

distributions as well as results from many other studies carried out over plant canopies in flat terrain (see Section 2.1.1). Due to directional shear, however, an upward moving air parcel transports a weaker upvalley component upwards and a sweep is connected with a stronger upvalley component which is transported into the canopy. The lateral momentum sweep is somewhat stronger than the ejection too.

Even though it is difficult to interpret 3-dimensional structures measured on a vertical profile only, an attempt is made to compare features that are expected to result from coherent structures at a slope, with the measured values. While Figure 4.8 shows the conditional averages

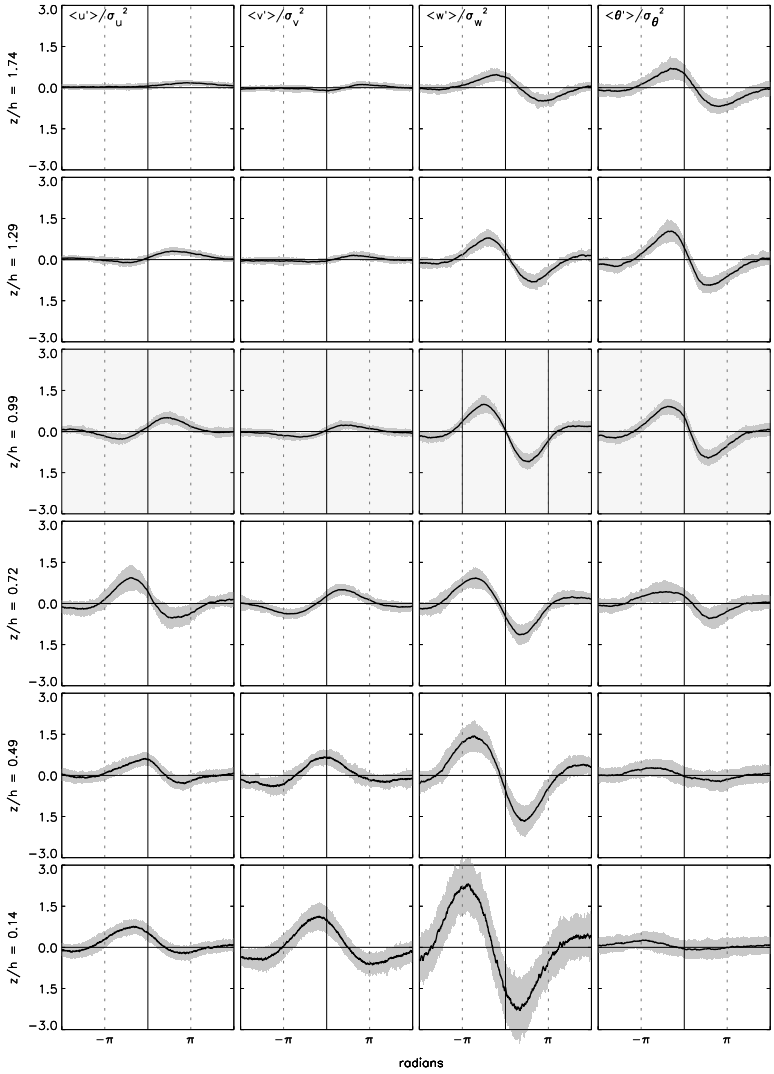

Fig. 4.8: Conditional averages of coherent structures. The reference level (z/h = 0.99) is shaded in light grey. Grey lines indicate the standard deviation between the runs and the black line stands for the mean value. Thin dashed lines delimit the period of the structure.

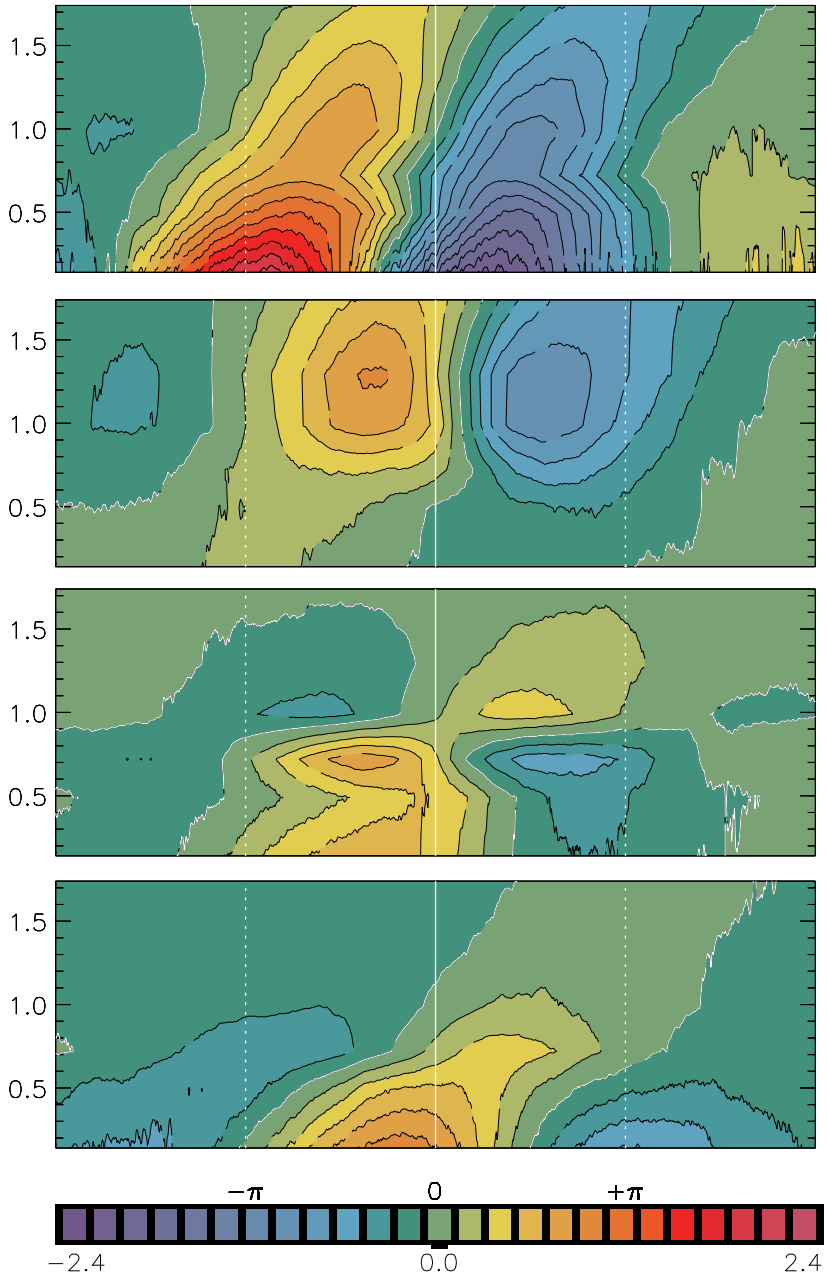

Fig: 4.9: Contour plot of perturbation in vertical velocity $\langle w' \rangle / \sigma_w^2$, temperature $\langle \theta' \rangle / \sigma_\theta^2$, longitudinal $\langle u' \rangle / \sigma_u^2$ and lateral velocity $\langle v' \rangle / \sigma_v^2$ in respective order. Thin dashed lines delimit the period of the structure and white isolines indicate zero crossing.

of each level Figure 4.9 shows contour plots of the observed structures. There is a lot of redundance between Figures 4.8 and 4.9 but both representations are shown, as they are more readable depending on whether the interest lies in profile information or in the temporal evolution of the structure.

A continuous phase shift is observed in the perturbation of the vertical velocity. Perturbations are first observed at the lowest level. By applying Taylors hypothesis it is possible to calculate the inclination angle of the structure advected along the measurement tower. The inclination calculated at the zero crossing of the structure amounts to 32° which is fairly close to the mean slope angle of 35°. This indicates, that the Kelvin Helmholtz instability leads to a disturbance that is - at least in its initial state - aligned with the streamlines and that the

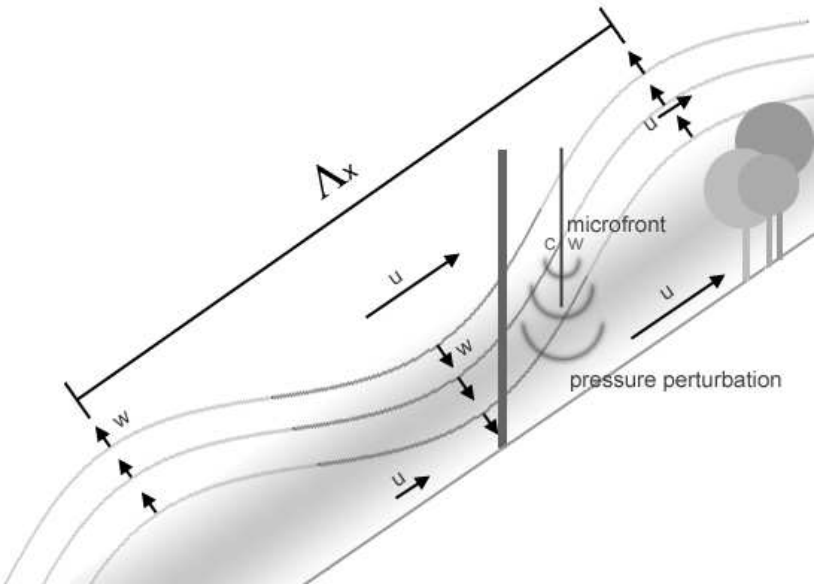

Fig. 4.10: Schematic of daytime canopy layer turbulence at a steep slope.

structure is moving at a constant speed, namely with the convection velocity U_c (see also Fig. 4.10).

Scalar fronts are usually inclined in the mean wind direction. Fig. 4.9b shows, that from z/h = 0.72 upwards no time delay appears in the measured temperature values. This indicates that the microfront is aligned to the geopotential and is thus inclined 35° with respect to the xy-plane.

Above the canopy, as already mentioned, a downward moving air parcel is connected with faster, more upvalley oriented,

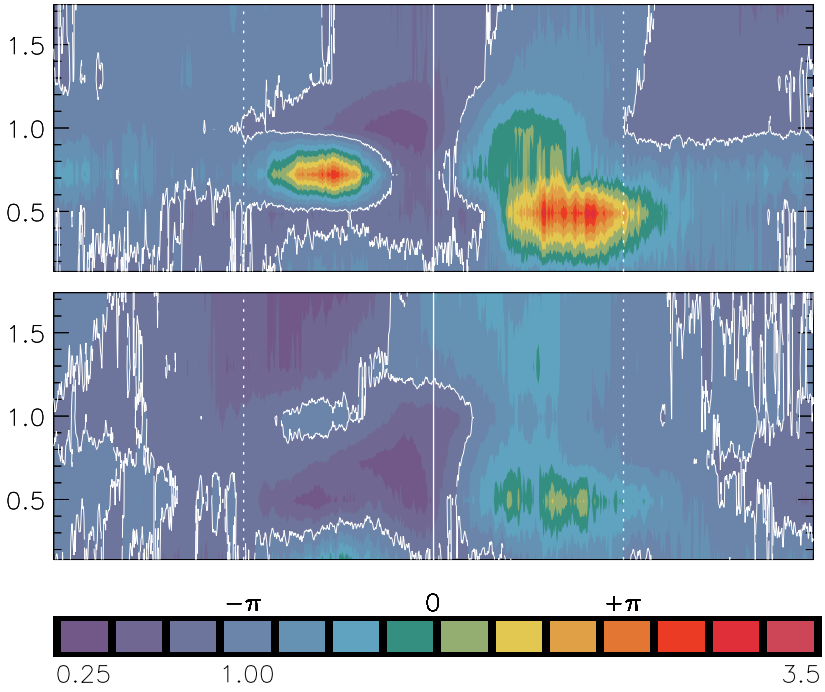

Fig. 4.11: Contour plot of conditional average of normalised momentum fluxes $\langle u'w' \rangle / \overline{u'w'}$ (top) and $\langle v'w' \rangle / \overline{v'w'}$ (bottom). Thin dashed lines delimit the period of the structure. For easier orientation the isoline where the ratio of conditional to Reynolds flux equals 1 is given as white line.

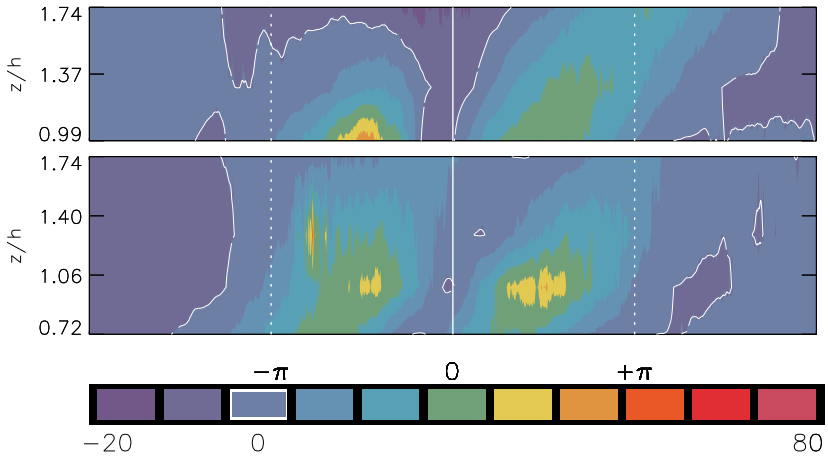

Fig. 4.12: Contour plot indicating the percentage fraction of the coherent part of the flux (top: $\langle u' \rangle \langle w' \rangle$ bottom: $\langle v' \rangle \langle w' \rangle$) to the conditionally averaged flux ($\langle u'w' \rangle$ and $\langle v'w' \rangle$ respectively).

colder air. Except for z/h = 0.72 the longitudinal and lateral signal generally show a continuous phase shift with height too. From canopy top to z/h = 0.72 the phase shift is almost 180°. The shift between the longitudinal and vertical signal in that level amounts to almost 90°, which confirms results from phase spectra, but can not easily be interpreted. At the lower levels, disturbances in both the longitudinal and the lateral velocity are increasingly phase shifted with respect to the vertical signal. Shaw and Zhang (1992) have shown, that accelerations at the ground of a (flat) forest occurred simultaneously to pressure perturbations (see also Section 2.1.1). In Figure 4.10 it is schematically depicted how a pressure perturbation can lead to a phase shift in the velocity signal between canopy top and trunk space. This phase shift in turn leads to the positive mean momentum fluxes in trunk space and for longitudinal momentum flux in z/h = 0.72 in the lower crown space too.

Figure 4.11 shows the ratio of the conditionally averaged momentum fluxes to the conventionally calculated Reynolds flux. Again with the exception of level z/h = 0.72 one can clearly see that the strongest positive deviations from the mean momentum fluxes occur during sweeps. In agreement with other studies this sweep dominance is increasing from the top level towards the canopy for longitudinal momentum fluxes.

Figure 4.12 shows the ratio of the coherent part of the flux and the conditional average of momentum fluxes. As in the canopy both, conditionally averaged and coherent fractions of the fluxes get too small for getting numerically stable ratios, only those levels with reasonably large fluxes are shown. At canopy top up to 60 % of the longitudinal and up to 70 % of the lateral momentum flux are made up by coherent structures. At z/h = 1.75 the coherent fraction of the flux is reduced to 30 % for the longitudinal and to 15 % for the lateral momentum flux indicating the limited vertical extension of these structures.

4.3 The stable boundary layer

4.3.1 Coherent structures

Diabatic effects on canopy flow are generally small. Due to the strong aerodynamic influence of roughness generally quite large deviations from neutral are necessary before buoyancy affects the flow Finnigan (2000). Brunet and Irvine (2000) argue, that the primary effect of atmospheric stability is to modify the shear length scale L_s through changes in $u(h)$ and $\mathrm{d}u / \mathrm{d}z_{z=h}$.

In the following a nighttime situation is presented where coherent structures are observed. It has to be mentioned, however, that the flow characteristics during this night are not typical. Usually wave-like structures of much larger length scale dominate the flow (see Section 4.3.2). The mean eddy separation distance Λ_x / h calculated from the peak frequency (eq. 4.5) amounts to 3.31. The slightly reduced mean eddy separation is in accord with Brunet and Irvine (2000), who found decreasing length scales with increasing stability due to an inhibition of turbulence by stability forces, resulting in velocity spectral peaks shifted to higher frequencies. During the time period analysed here weakly stable conditions were met with $0.5 > h/L > 0.05$ at the uppermost level.

In the night of August 22 to 23 an anticyclone to the west of Brittany lead to fairly southerly flow in the Riviera valley which turned

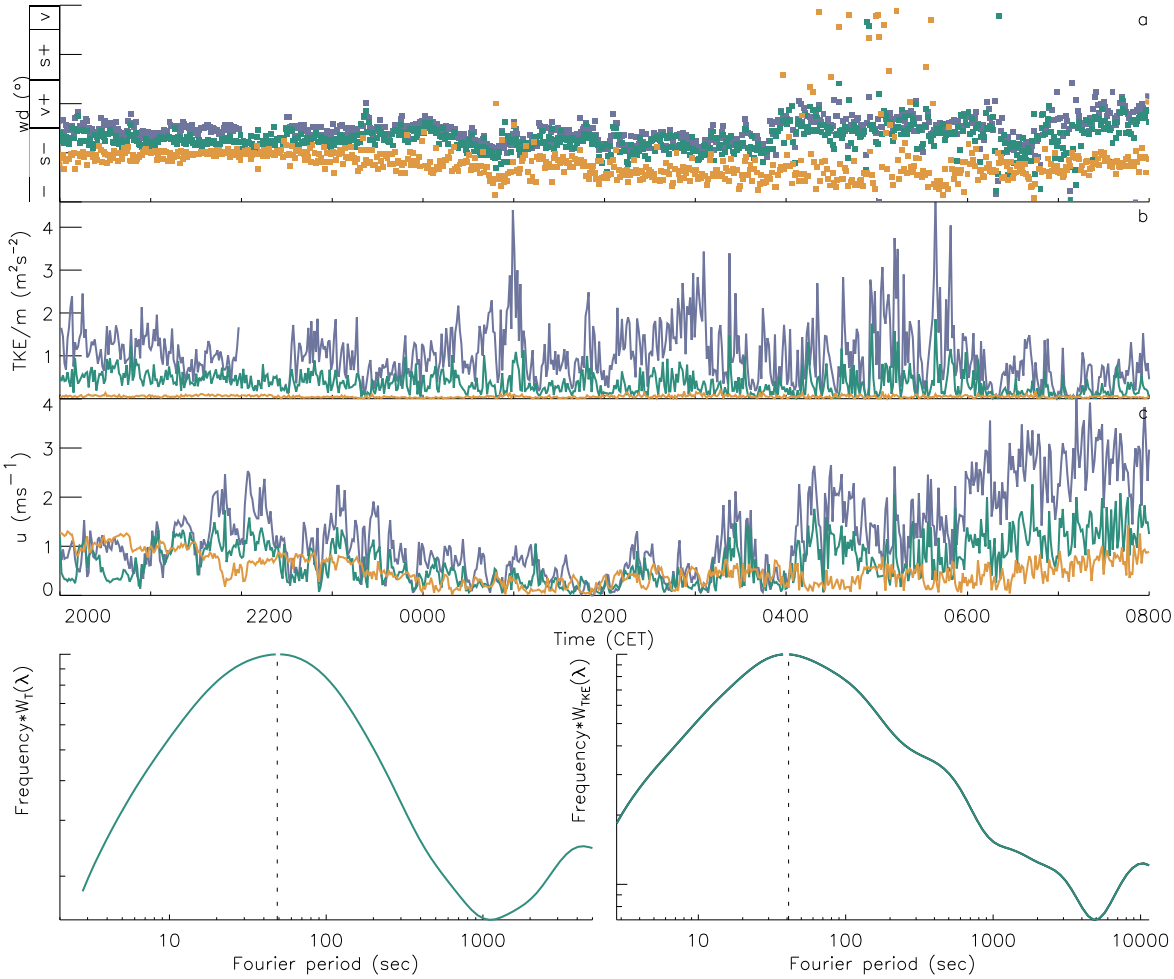

Fig. 4.13: Time series of 1 minute block averages of a) wind direction b) turbulent kinetic energy per mass, c) wind velocity. Furthermore global wavelet spectra calculated of 1 sec block averages of temperature and TKE are shown for $z/h = 0.99$.
Colours are used as follows: orange, green and blue lines and symbols stand for measurements at $z/h = 0.14$, 0.99 and 1.74 respectively. In Figure 4.13a *v* stands for valley and *s* for slope and + and – indicate upward and downward respectively.

to southwesterly flow on August 23. Figure 4.13 gives an overview over some important flow characteristics that prevailed in the night of August 22 to 23. Wind direction is fairly steady until 0400 CET. During the whole time period there is directional shear. The still prevailing upvalley component present at the topmost level decreases with decreasing height. At the lowest level there is a plain downslope wind. From 0400 CET on there is a shift in wind direction towards more upvalley winds at the upper levels. Wind velocity and standard deviations of wind direction increase while TKE is lowered in the early morning hours. Temperature spectral power (calculated from 1 s mean data over the whole time period) has a maximum at roughly 50

Tab. 4.6: Ratio of conditional average of longitudinal and lateral momentum flux to conventionally calculated Reynolds flux.

z/h	$\frac{1}{N}\sum_N \frac{\overline{\langle u'w' \rangle}}{\overline{u'w'}}$	$\frac{1}{N}\sum_N \frac{\overline{\langle v'w' \rangle}}{\overline{v'w'}}$
1.74	1.02	1.00
1.29	1.02	1.03
0.99	1.03	1.06
0.72	0.98	1.01
0.49	1.00	1.07
0.14	0.96	0.92

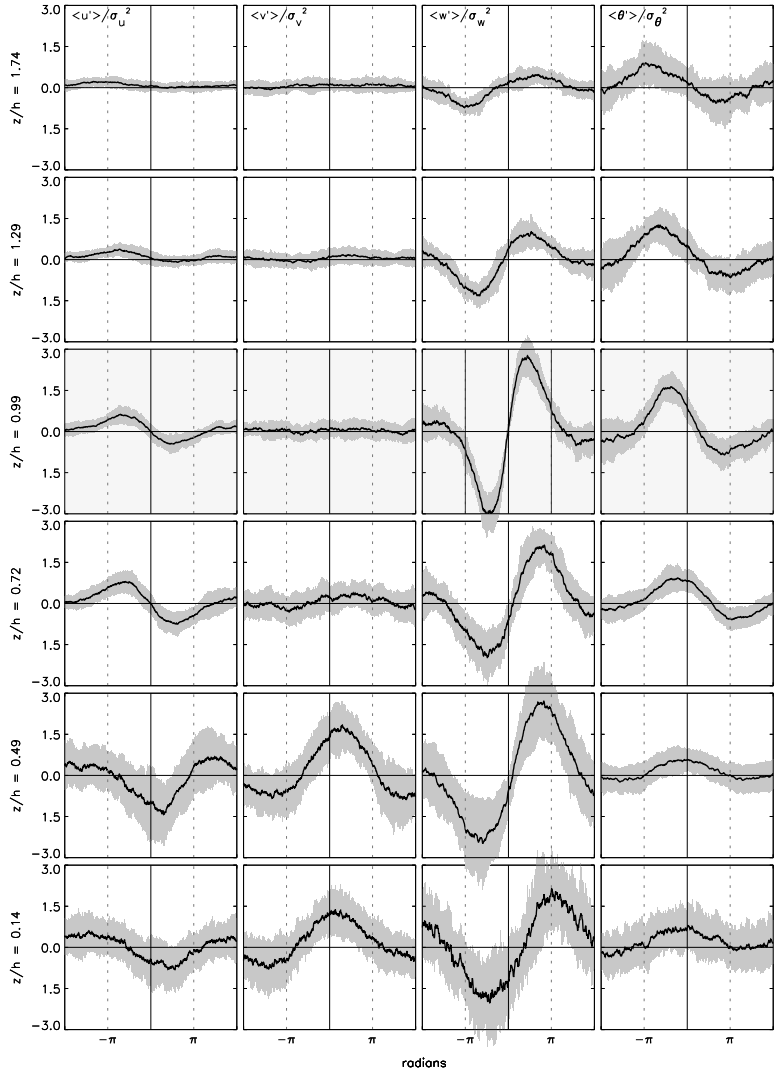

Fig. 4.14: Conditional averages of coherent structures. The reference level (z/h = 0.99) is shaded in light grey. Grey lines indicate the standard deviation between the runs and the black line stands for the mean value. Thin dashed lines delimit the period of the structure.

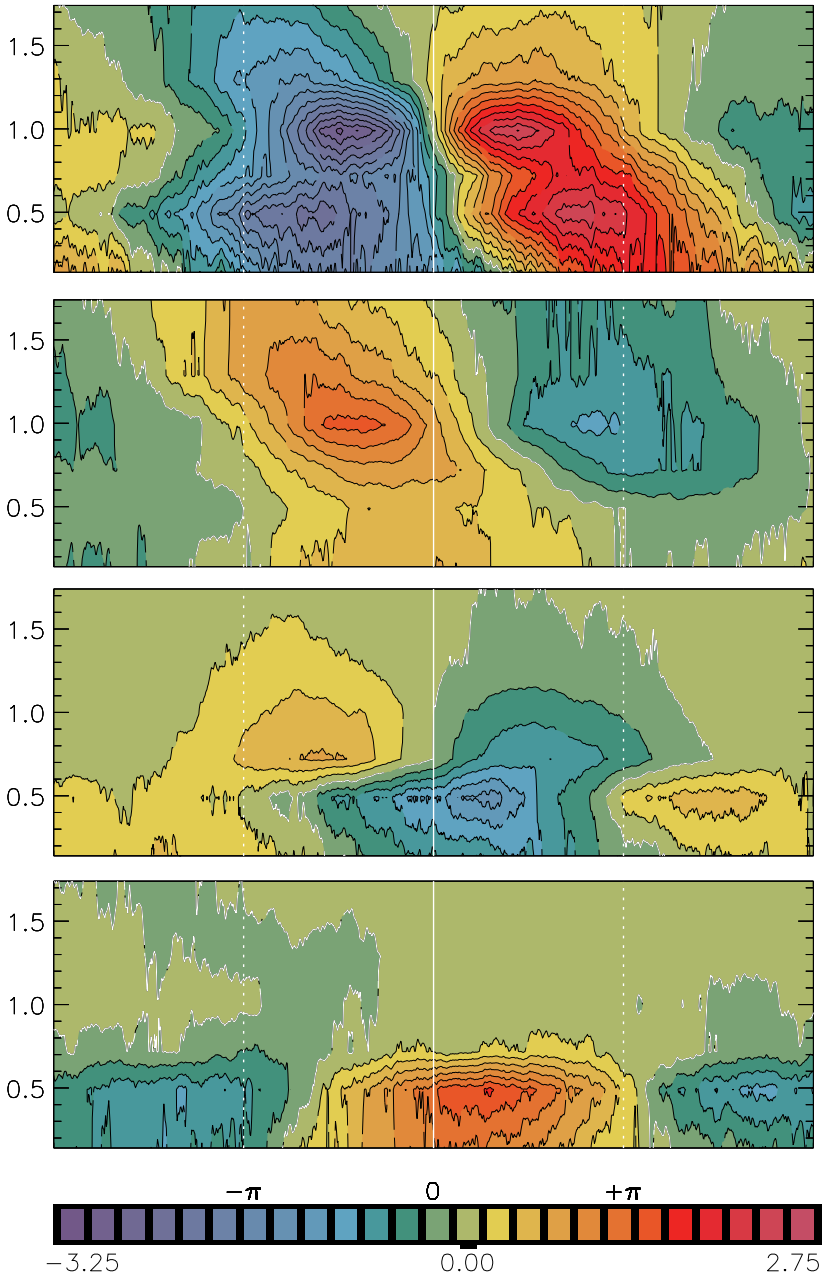

Fig: 4.15: Contour plot of perturbation in vertical velocity $\langle w' \rangle / \sigma_w^2$, temperature $\langle \theta' \rangle / \sigma_\theta^2$, longitudinal $\langle u' \rangle / \sigma_u^2$ and lateral velocity $\langle v' \rangle / \sigma_v^2$ in respective order. Thin dashed lines delimit the period of the structure and white isolines indicate zero crossing.

seconds, while TKE spectral power peaks at roughly 40 seconds. The peak frequencies of *u, v,* and *w* lie at 50, 40, and 17 seconds respectively (not shown).

As during daytime the Reynolds stresses of momentum are fairly well represented by the conditional averages of the flow (Tab. 4.6).

Figure 4.14 shows the conditional averages of the coherent structures. Contrary to the daytime situation where cold faster moving air is swept into the canopy and is thereby building a cold microfront, the faster air that penetrates the canopy at night is relatively warm and causes a warm microfront. The normalised standard deviations of vertical velocity and temperature are much larger than during

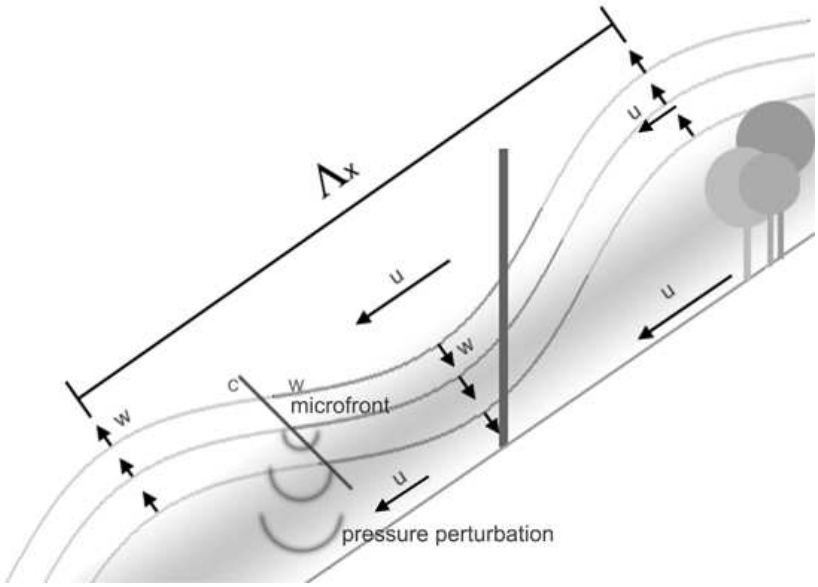

Fig. 4.16: Schematic of nighttime canopy layer turbulence at a steep slope.

daytime, whereas longitudinal and lateral movements are suppressed.

Similar to daytime conditions a continuous phase shift is observed in the positive perturbation of the vertical velocity signal. Calculation of the inclination angle at the zero crossing of the structure amounts to 38° indicating that the structure is fairly parallel to the slope. Negative deviations however occur fairly simultaneously. This leads to an asymmetric structure with ejections following the geopotential and sweeps the slope normal.

The temperature microfront is slightly inclined in the mean wind direction. The inclination averages to 46° and therefore roughly deviates 10° with respect to the streamline.

Longitudinal and lateral velocity perturbations show characteristics we would expect if there was a pressure perturbation propagating through the canopy. Namely if there is a pressure perturbation ahead of the advancing microfront we would expect to observe a deceleration of the longitudinal component in trunk space connected with a lateral drain off of

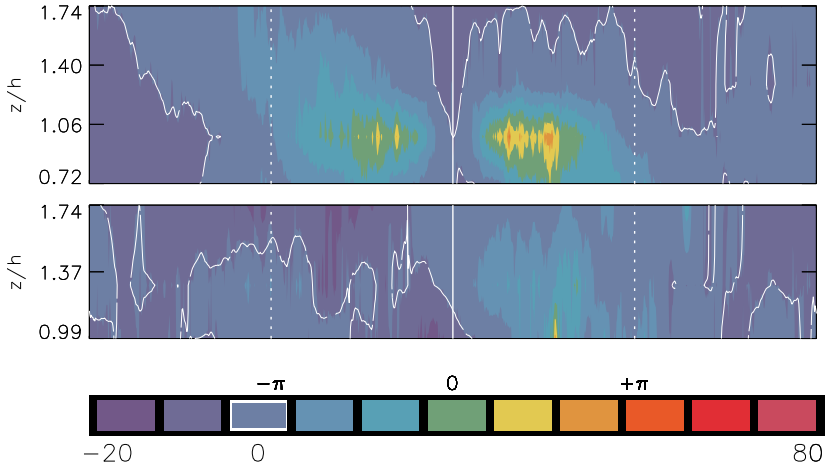

Fig. 4.17: Contour plot indicating the percentage fraction of the coherent part of the flux (top: $\langle u' \rangle \langle w' \rangle$ bottom: $\langle v' \rangle \langle w' \rangle$) to the conditionally averaged flux ($\langle u'w' \rangle$ and $\langle v'w' \rangle$ respectively).

the air masses (see also Fig. 4.16). Thus while there is relatively fast moving air at canopy top top and above, the flow in trunk space is decelerated in longitudinal direction. At the time when the negative longitudinal velocity perturbation is at maximum the lateral perturbation is largest. Perturbations in the lateral signal are observed in trunk space only.

Deviations between conditional averages of $\langle u'w' \rangle, \langle v'w' \rangle$ and the conventionally averaged Reynolds fluxes are much smaller than during daytime (not shown). That the structures are limited in their vertical extension is also shown in Figure 4.17. At canopy top still up to 60% of the longitudinal but only up to 30 % of the lateral flux result from coherent structrues.

4.3.2 Wave like characteristics

As mentioned in Section 4.3.1 nighttime flows in the Riviera valley are characterised by wave like structures of relatively large scale. Many other observations of nocturnal drainage flows have indicated that oscillations with periods between 10 to 90 min are frequently observed in katabatic winds (see also Section 2.1.2). These oscillations are usually attributed either to compressional warming (Fleagle, 1950; McNider, 1982; Doran and Horst, 1981) or to modulations of the flow by gravity waves (Gryning et al., 1985; Stone and Hoard, 1989).

Nocturnal drainage flows are often accompanied by surges which manifest themselves as fluctuations of wind velocity. Figure 4.18 shows a time series of the slope wind component (u_s), wind direction and potential temperature (θ). It gives a first impression of the flow characteristics observed at station E2 above the forest. One can easily make out three to four periods per hour in velocity and temperature

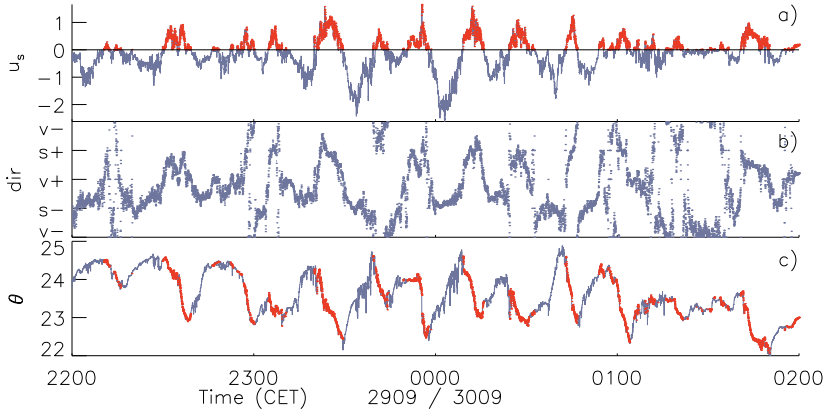

Fig. 4.18: Time series showing 1 sec block means of station E2 at $z/h = 1.74$ of a) slope wind component (positive values: upslope), b) wind direction (v stand for valley, s for slope, + for up and – for down) and c) potential temperature. For easier orientation values where u_s is positive are marked with red dots.

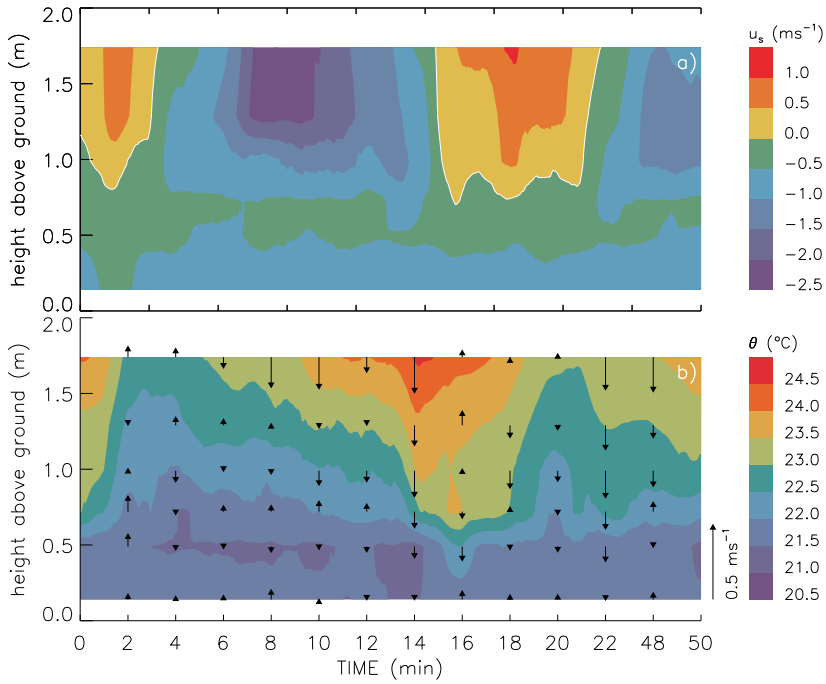

Fig. 4.19: Vertical profile of a) u_s (white line indicates the zero isoline) and b) vertical wind component (arrows) and temperature.

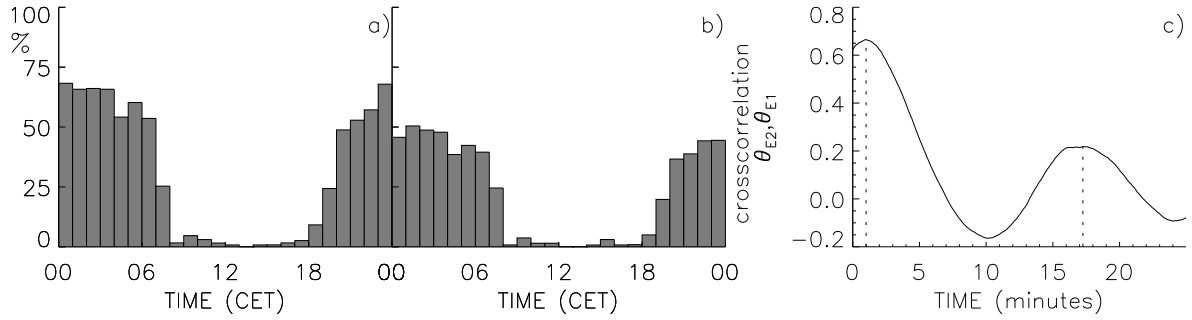

Fig. 4.20: Percentage of hours where temperature drops were detected in the temperature signal. Analysis has been carried out for the whole measuring period (01.08.1999-10.10.1999) a) station E2, b) coherent events at stations E2 and E1 c) cross correlation of temperature signal between stations E2 and E1. A four hour period was used for calculating the cross correlation (September 29 / 30, 2200-0200).

signals, and spectral analysis indicates, that the peak frequency of temperature and u_s is 15 and 14 min respectively. The wind direction is highly variable and winds are often directed slope upwards for several minutes. Connected with a positive slope wind component are decreasing temperatures and vice versa, which is supportive of theory of compressional warming (Fleagle, 1950): radiative cooling of sloping surfaces causes the adjacent air to cool more than the free air at the same elevation, resulting in a downslope flow. However, as the air moves downslope, compressional warming reduces temperature deficit and pressure gradient. Adiabatic heating then exceeds radiative cooling and results in a reversal of the pressure gradient. As the air decelerates, friction decreases, and radiative cooling increases the pressure gradient. The cycle then is repeated.

As the area of radiative energy exchange is located in the upper region of the crown space we might expect to observe these surges mainly around canopy top. Figure 4.19 shows, that fluctuations in the slope wind component are indeed mainly confined to measurements carried out from within crown space upwards. The increasing amplitude with height can easily be explained with decreasing friction. In the lower canopy and in trunk space a fairly steady cold air drainage is observed. However, vertical velocity and temperature field (Fig. 4.1.9b) indicate, that relatively warm air is mixed into the canopy just before the onset of upslope flows. Even though this is shown only exemplarily here, this is a regularly observed exchange mechanism of the nighttime flow.

Having oscillations of relatively large scale we expect to find similar flow features at other stations. Figure 4.20 indicates the percentage of hours where wave like structures have been observed either at station E2 or simultaneously at stations E2 and E1. For the detection of these oscillations 1 hour time series of 1 s block means of the temperature signal have been used. Calculations of the auto correlation (cross correlation) of station E2 (E2 / E1) were carried out and were searched for a second maximum in the interval of 10 to 25 minutes. The correlation of the temperature signal between the stations often reaches very high values (Fig. 4.20c) and it is confirmed, that these oscillations are a very common feature of the nighttime flow (occurrence in roughly 70% of all nights) and that they often occur coherently at both stations (50%).

In the following the flow characteristics of the night from September 29 to 30 are analysed. The choice of this time period is rather pragmatic as on one hand during this night oscillations were observed and on the other hand additional data from radiosondes and MTP5 temperature profiles were available. Figure 4.21 gives an overview of the same variables as given in Section 4.3.1. One can easily see that, while the wind direction at the lowest level is fairly constant and downslope until 0600 CET, the wind direction at the upper levels is highly variable. Levels of turbulent kinetic energy at canopy top and above are generally lower than during the night of August 22 to 23, but especially in the first half of the night it is possible to make out roughly four periods per hour. Highest wind velocities are observed at the lowest measurement level. There is a fairly persistent cold air drainage in trunk space, whereas in the upper levels a strong variability in all velocity components can be observed. This is

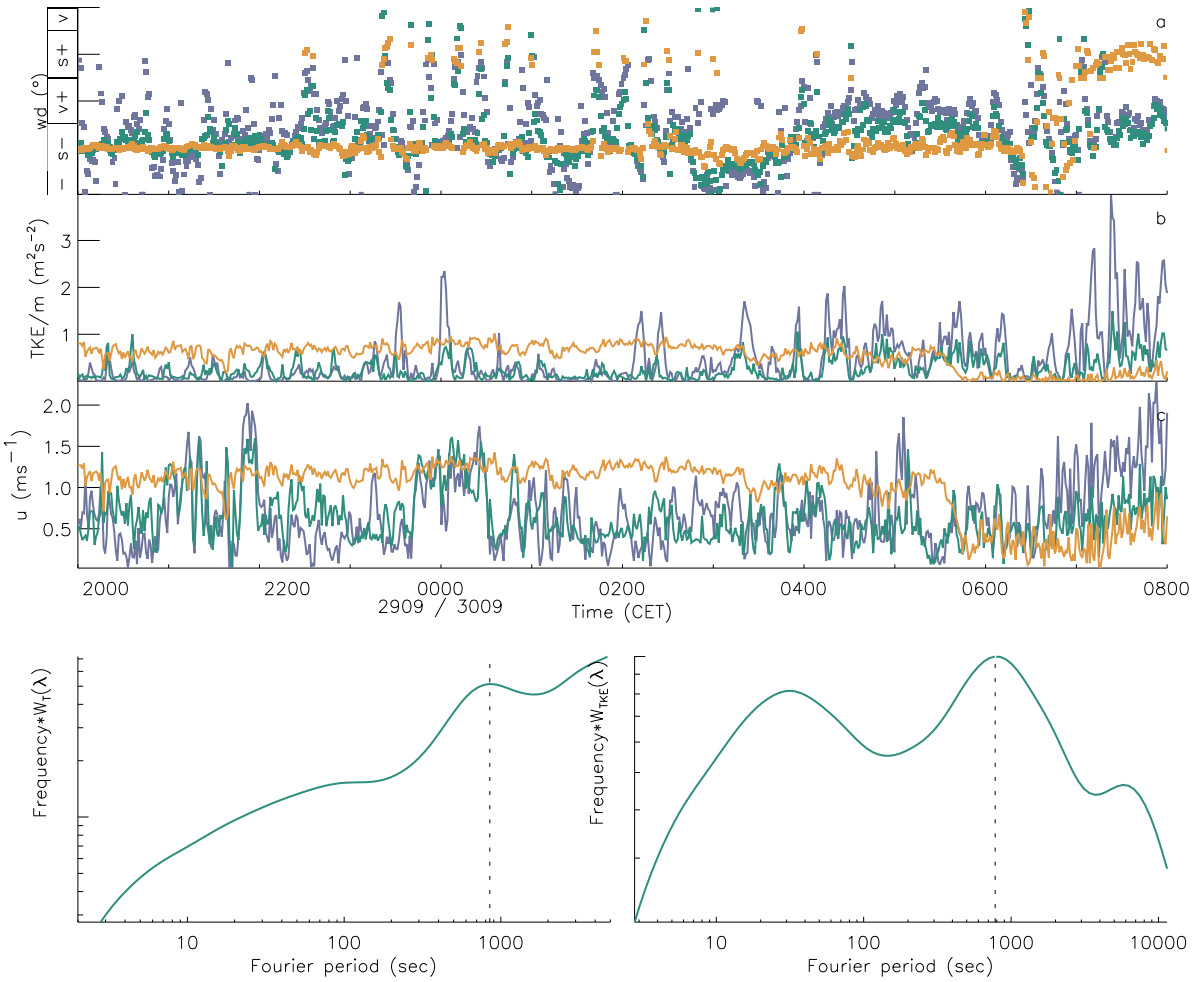

Fig. 4.21: Time series of 1 min block averages of a) wind direction b) turbulent kinetic energy per mass, c) wind velocity. Furthermore global wavelet spectra calculated of 1 sec block averages of temperature and TKE are shown for z/h = 0.99.
Colours are used as follows: orange, green and blue lines and symbols stand for measurements at z/h = 0.14, 0.99 and 1.74 respectively. In Figure 4.21a *v* stands for valley and *s* for slope and + and – indicate upward and downward respectively.

also confirmed by the spectra of temperature and TKE which have a (relative) maximum at 15 and 13 minutes respectively.

Figure 4.22 shows measurements of the radiosonde of September 29 started at 2356 CET. One can discern three layers. From the valley floor up to 1250 m a.s.l there is a relatively strong temperature increase with height. The higher valley atmosphere is stratified more isothermal and above the mountain ridge there is a secondary increase in the potential temperature. Wind velocities in the valley are moderate and increase markedly only above mountain ridge height. Richardson numbers indicate that the atmosphere is susceptible to gravity waves (Ri<0.25). With a simple approach to model internal gravity waves (e.g Haltiner, 1971; Gryning et al., 1985) we calculate the oscillation period to be 18 min. The model relates the period P of oscillations to the horizontal length scale (L) and the height of the valley (H) by

$$P = 2\pi / N\left[1 + (L/H)^2\right]^{0.5} \qquad (4.6)$$

where N is the Brunt-Väisälä frequency and is computed for the whole valley atmosphere. The wind direction in the valley (Fig. 4.22b) changed from southerly flow in the afternoon of September 29 (upvalley wind) to northerly flow (downvalley wind) in the night while in the upper valley winds were directed upvalley during the

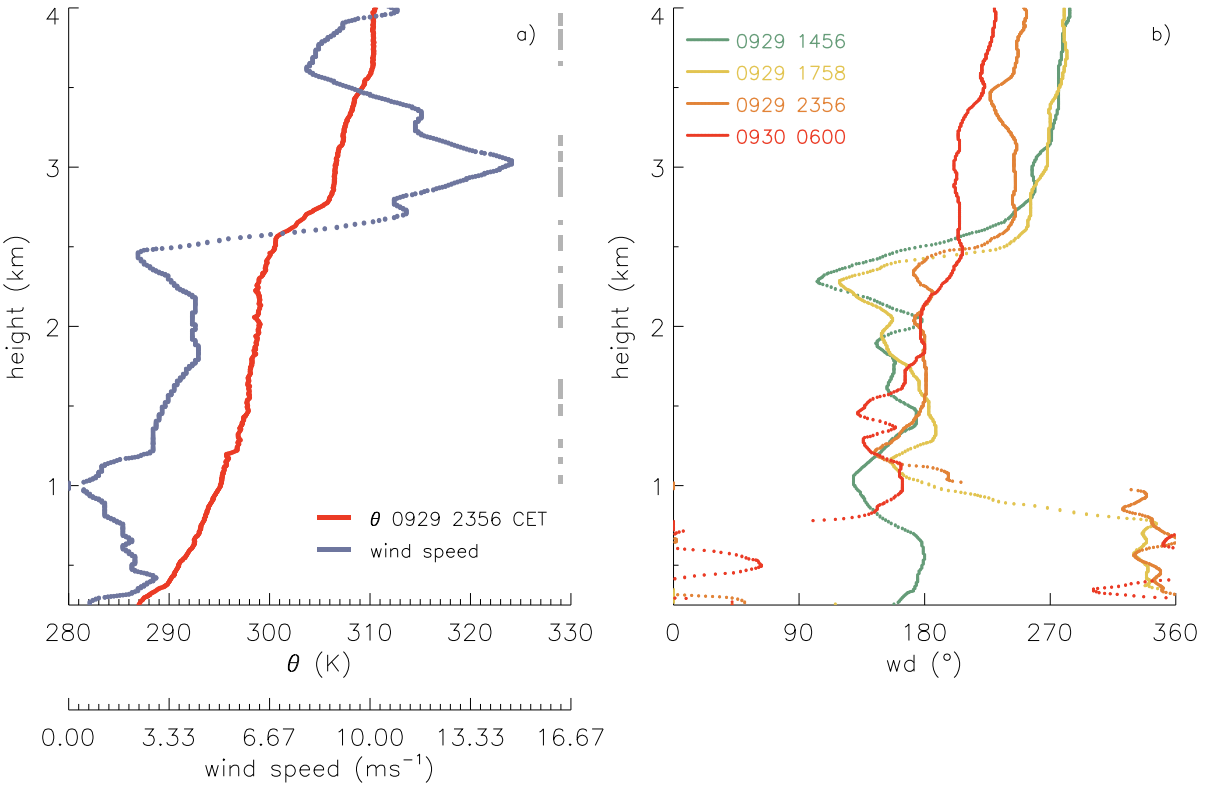

Fig. 4.22: Vertical profile of potential temperature and wind speed from the radiosonde of September 29 started at 2356 CET. Grey symbols at the very right indicate where the Richardson number is <0.25. b) Vertical profiles of wind direction.

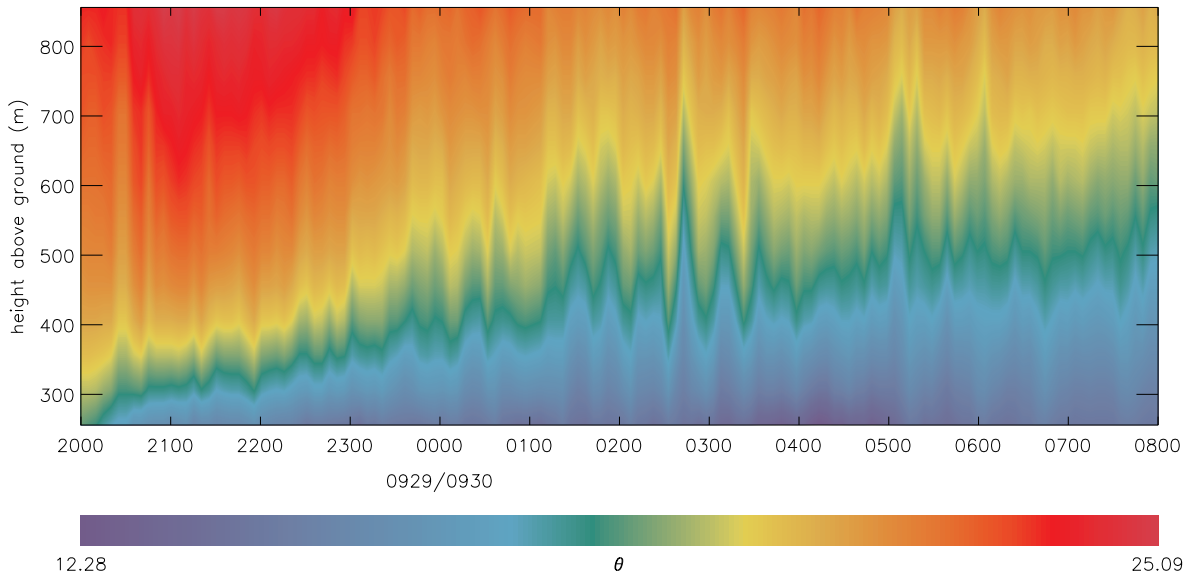

Fig. 4.23: Contour plot of vertical profiles of potential temperature measured with MTP5.

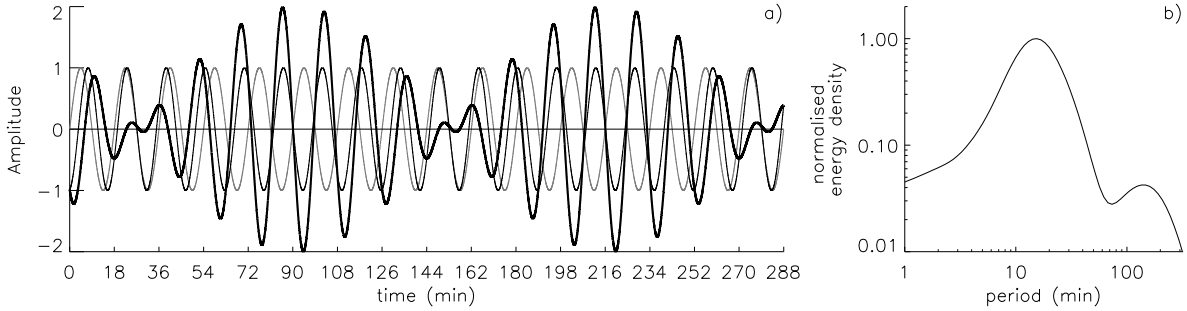

Fig. 4.24: a) Schematic of interference between valley (grey line) and slope temperature (thin black line). The resulting temperature difference is given as black thick line. b) Global wavelet spectrum of slope wind component (E2).

whole time period. Above ridge height wind direction changed from a westerly to a more southern flow. The profiles of wind velocity and wind direction indicate strong shear between these three layers.

Figure 4.23 shows vertical profiles of the potential temperature, measured with a meteorological temperature profiler (MTP5). One can clearly see the growing of the cold air layer on the valley floor with time. More interesting are the wave like structures that are discernable in the valley atmosphere during almost the whole night. These structures are in phase through the whole layer and thus stationary relative to the ground, which is indicative for terrain generated waves. The period of these waves (18 min) is somewhat larger than those observed at the slope but is equal to the period modeled with radiosonde data.

There is a phase shift of roughly 3.5 min between the valley and the slope temperature. Temperatures in the valley core and at slopes interfere such, that difference maxima are reached roughly every 120 min (Fig. 4.24). At approximately this period (130 min) a secondary maximum is found in the spectrum of slope winds. This indicates, that slope and valley flow oscillations are not independent and that waves may enhance or suppress oscillations caused by compressional warming.

In summary it was shown that there is evidence for compressional warming being a cause of oscillations in katabatic flows in the Riviera valley. Radiosonde and MTP5 measurements however indicate that wave like structures in the valley core might be induced by dynamic instabilities. It is proposed that internal gravity waves may enhance / suppress slope boundary layer oscillations and by doing so strongly modify the exchange of momentum and scalars.

5 Summery and conclusions

research objective: the MAP-RIVIERA project primarily aimed at helping to fill the gap of knowledge on turbulence structure in complex terrain. The field study was very successful and provided a valuable data set resulting from ground based and remote measurements. In this thesis aspects of slope boundary layer turbulence and of energy distribution and exchange mechanisms between slope boundary layer and valley atmosphere are discussed.

turbulence above a steep forested slope: In the neutral and weak unstable slope boundary layer velocity profiles have an inflection point near the top of the canopy, which leads to instability processes and turbulence characteristics similar to those in a canopy layer in flat terrain. This can not be anticipated as model simulations and wind tunnel experiments of flow over forested hills (Finnigan and Brunet, 1995; Finnigan and Belcher, 2002) have indicated, that differences in the response to the imposed pressure gradient deep in the canopy and above, can lead to a reduction of canopy-top shear on the upwind slope. The reason for the maintenance of the inflection point should not primarily lie in the steepness of topography. Even though the application of linearised models may be doubtful for such terrain, one would expect even larger pressure perturbations and an enhancement of the above described effect. It is more likely that the inflection in the wind profile is maintained due to the three dimensionality of the flow. Pressure gradients develop in upvalley and upslope direction and lead to longitudinal and lateral shear that are in the same order of magnitude. Whereas the longitudinal shear has a maximum at canopy top, lateral shear decreases continuously. Shear instabilities lead to the development of coherent eddies. Length scales derived from autocorrelation and spectral analysis show that the eddies, dominating the turbulence structure of canopy flow, are in the order of 50 m during daytime conditions, which corresponds fairly well to length scales observed in same sized medium dense forests above flat terrain. The peak frequency of spectra is fairly constant through the canopy confirming that eddies occupying the whole canopy, dominate the turbulence structure. At canopy top coherent structures account for up to 60% of the longitudinal and up to 70% of the lateral momentum flux. On the low frequency side of u- and v-spectra remarkably little disturbances are observed. Contrary to turbulence over flat terrain large scale longitudinal and lateral fluctuations seem to be suppressed. Large scale eddies might thus be topographically forced to remain quite stationary leading to a fairly sharp separation between mean flow characteristics and turbulence. Above the canopy, in the roughness sublayer, energy is removed from the mean flow and injected into coherent eddies. In the canopy work is done against pressure drag and against the viscous component of canopy drag. Kinetic energy is then directly converted into fine-scale wake turbulence and heat, respectively. These processes extract energy from the mean flow and from eddies of all scales larger than the canopy elements. They are most obvious in vertical velocity spectra and are typical of canopy flows. Apart from decreasing TKE levels we observe decreasing momentum fluxes resulting on the one hand from the absorption of momentum as aerodynamic drag on the foliage too, on the other hand an increasing phase shift between the velocity signals leads to a decorralation between them, this not only in the inertial subrange, but also at relatively large scales. It seems plausible, that pressure perturbations, resulting from a convergence of the flow at canopy top and propagating vertically at the speed of sound, lead to an redistribution and increase of TKE with velocity components being fairly uncorrelated.

In the (weakly) stable boundary layer one could expect coherent eddies too. However, they are observed on rare occasions only, as the energy exchange usually takes place on much larger scales. The mean eddy separation distance in the weakly stable case is 43 m; the slightly reduced mean eddy separation being in accord with an inhibition of turbulence due to stability forces. At canopy top up to 60% of the longitudinal but only up to 30% of the lateral momentum flux are caused by coherent structures. At $z/h = 1.74$ the coherent fraction of the flux is insignificant, indicating that nighttime coherent structures are limited in their vertical extension to about $1.5h$ only.

wave like characteristics: surges, resulting in fluctuations of wind velocity are an

often observed feature in katabatic flows. The reason for these oscillations, which usually have periods between 10 and 90 minutes, is not fully clear but the oscillations are mainly explained either with compressional warming or with gravity waves. In the Riviera valley oscillations with periods between 10 and 25 min are observed in roughly 70% of all nights. They mainly occur coherently at different stations on the slope (50% of all nights). Increasing temperatures that are connected with downslope winds and vice versa indicate that compressional warming is a trigger mechanism of occurring upslope flows. Further support is given by the fact that oscillations are strongest above the canopy, where the area of radiative exchange is located. Furthermore periods expected to result from internal gravity waves are somewhat longer than those observed in the downslope flow. On the other hand, the down-valley flow in the bulk of the valley atmosphere exhibits a periodicity very close to that expected for internal gravity waves. Consequently, interfering temperature fluctuations between the downslope and the downvalley flows result in a secondary energy maximum in downslope flows, indicating that gravity waves may enhance or suppress exchange mechanisms at the slope.

implications: during daytime conditions surprisingly many characteristic features of both, canopy and mixing layers are observed. As large scale pressure perturbations do not reduce canopy-top shear to the point that shear instabilities are not initiated, coherent structures are responsible for much of the turbulent exchange. Length scales are very close to what we know from turbulence in forests above flat terrain. Main differences resulting from the complex terrain are directional shear, which is caused by the superposition of the slope and valley wind system, and a lack of low frequency disturbances in the slope parallel wind components, which may be attributable to large scale eddies that are topographically forced to remain stationary.

During nighttime exchange mechanisms are much more influenced by topography. Only in rare cases, supposedly when valley inversions are weak and synoptic winds in a more valley parallel direction, canopy layer flow characteristics are observed. On the majority exchange takes place on fairly large scales and turbulence levels are low. Oscillations in katabatic winds are observed that are associated with downmixing of warm air into the canopy and that are interacting with topographically induced waves.

References:

Amiro, B.D.: 1990, 'Drag Coefficients and Turbulence Spectra within Three Boreal Forest Canopies.' *Boundary-Layer Meteorol.*, 52, 227-246.

Arya, S.P.: 2001, *Introduction to Micrometeorology*, Academic Press, San Diego (Calif.), 2nd ed., 420 pp.

Baldocchi, D.D. and Hutchison, B.A.: 1987, 'Turbulence in an Almond Orchard: Vertical Variations in Turbulent Statistics.' *Boundary- Layer Meteorol*., 40, 127-146.

Barry, R.G.: 1992, *Mountain Weather & Climate*, Routledge, London and New York, 2nd ed., 402 pp.

Biltoft, A.: 2001, 'The Kolmogorov and Taylor Hypothesis Revisited.' *11th Symposium on Meteorological Observations, Albuquerque, NM*, Jan. 14-19, 2001, American Meteorological Society, 45 Beacon St., Boston, MA, pp. 24-28.

Bradley, E.F.: 1980, 'An Experimental Study of the Profiles of Wind Speed, Shearing Stress and Turbulent Intensities at the Crest of a Large Hill.' *Q.J.R Meteorol. Soc.*, 106, 101-124.

Brunet, Y. and Irvine, M.R.: 2000, 'The Control of Coherent Eddies in Vegetation Canopies: Streamwise Structure Spacing, Canopy Shear Scale and Atmospheric Stability.' *Boundary-Layer Meteorol.*, 94, 139-163.

Businger, J.A.: 1982, 'Equations and Concepts', in F:T:M. Nieuwstadt and H. Van Dop (ed.), *Atmospheric Turbulence and Air Pollution Modelling. A Course Held in The Hague.*, 21-25 September, 1881, (D. Reidel; distributed by Kluwer), Boston, MA, pp. 358.

Christen, A., van Gorsel, E., Andretta, M., Calanca, P., Rotach, M.W. and Vogt, R.: 2000, 'Intercomparison of Ultrasonic Anemomemeters during the MAP-Riviera Project.' *Ninth Conference on Mountain Meteorology, Aspen, Co.*, Aug, 7-11, 2000, American Meteorological Society,45 Beacon St., Boston, MA, pp. 130-131.

Collineau, S. and Brunet, Y.: 1993a, 'Detection of Turbulent Coherent Motions in a Forest Canopy Part 1: Wavelet Analysis.' Boundary-Layer Meteorol., 65, 49-73.

Collineau, S. and Brunet, Y.: 1993b, 'Detection of Turbulent Coherent Motions in a Forest Canopy Part 1: Time Scales and Conditional Averages.' Boundary-Layer Meteorol., 66, 49-73.

Coulter, R.L., Oriel, M. and Porch, W.M.: 1989, 'Tributary fluxes into Brush Creek Valley.' J.Appl.Meteorol., 28, 555-568.

Daubechies, I.: *Ten Lectures on Wavelets*, Society for Industrial and Applied Mathematics, Philadelphia, 357 pp.

De Bruin, H.A.R., Kohsiek, W. and van den Hurk, B.J.J.M.: 1993, 'A Verification of some Methods to Determine the Fluxes of Momentum, Sensible Heat and Water Vapour Using Standard Deviation and Structure Parameter of Scalar Meteorological Quantities.' *Boundary-Layer Meteorol*., 63, 231-257.

Doran, J.C. and Horst, T.W.: 1981, 'Velocity and Temperature Oscillations in Drainage Winds.', *J.Appl.Meteorol.*, 20, 361-364.

Egger, J: 1990, 'Thermally Forced Flows: Theory', In: W. Blumen (ed.), *Atmospheric Processes over Complex Terrain*, 23, American Meteorological Society, Boston, MA, pp.43-57.

Feigenwinter, Ch.: 1995, 'The Vertical Structure of Turbulence above an Urban Canopy', Dissertation, University of Basel, Basel, 76 pp.

Feigenwinter, Ch., Vogt, R. and Parlow, E.: 1999, 'Vertical Structure of Selected Turbulence Characteristics above an

Urban Canopy.' *Theor.Appl.Climatol.*, 62, 51-63.

Finnigan, J.J. and Belcher, S.E.: 2002, 'Flow over a hill covered with a plant canopy.', Submitted to *Q.J.R.Meteorol.Soc.*

Finnigan, J.J. and Belcher, S.E.: 2000, 'An Analytical Model of Airflow over and within a Tall Canopy on a Low Hill.' *24th conference on agricultural and forest meteorology*, Davis, C.A., Nov. 23-25, 2000, pp. 200-210.

Finnigan, J.J. and Shaw, R.H.: 2000,'A Wind Tunnel Study of Airflow in Waving Wheat: An EOF Analysis of the Structure of the Large-Eddy Motion', *Boundary-Layer Meteorol.*, 96, 211-255.

Finnigan, J.J. and Brunet, Y.: 1995, 'Turbulent Airflow in Forests on Flat and Hilly Terrain', In: M.P. Coutts and J. Grace (ed.), *Wind and Trees*, Cambridge University Press, Cambridge, pp.3-40.

Finnigan, J.J., Raupach, M.R., Bradley, E.F. and Aldiss, G.K.: 1990, 'A Wind Tunnel Study of Turbulent Flow over a Two-Dimensional Ridge', *Boundary-Layer Meteorol.*, 50, 277-317.

Fleagle, R.G.: 1950, 'A Theory of Air Drainage', *J.Meteor.*, 7, 227-232.

Gao, W., Shaw, R.H. and PawU, K.T.: 1992, 'Conditional Analysis of Temperature and Humidity Microfronts and Ejection/Sweep Motions within and above a Deciduous Forest.' *Boundary-Layer Meteorol.*, 59, 35-57.

Gryning, S.E., Mahrt, L. and Larsen, S.: 1985, 'Oscillating Nocturnal Slope Flow in a Coastal Valley.' *Tellus*, Series A, 37A(2), 196-203.

Jackson, P.S. and Hunt, J.C.R.: 1975, 'Turbulent Wind Flow over a Hill.' *Q.J.R.Meteorol.Soc.*, 101, 929-955.

Kaimal, J.C. and Finnigan, J.J.: 1994, *Atmosperic Boundary Layer Flows*, Oxford Univ. Press, Oxford, 289 pp.

Kaimal, J.C.: 1978, 'Horizontal Velocity Spectra in an Unstable Surface Layer', *J.Atm.Sci.*,35, 18-24.

Katul, G.G., Lai, C.T., Schäfer, K. Vidakovic, B. Albertson, J., Ellsworth, D. and Oren, R.: 2001, 'Multiscale Analysis of Vegetation Surface Fluxes: From Seconds to Years.' *Advances in Water Research*, 24, 1119-1132.

Kolmogorov, A.N.: 1962, 'A refinement of Previous Hypothesis Concerning the Local Structure of Turbulence in a Viscous Incompressible Fluid at High Reynolds Number.' *J.Fluid.Mech.*, 13, 82-85.

Kolmogorov, A.N.: 1941, 'Dissipation of Energy in Locally Isotropic Turbulence', *Dokl.Akad.Nauk.SSSR*, 32, 16-18.

Kruijt, B., Malhi, Y., Lloyd, J., Nobre, A.D., Miranda, A.C. and Pereira, M.G.P.: 2000, 'Turbulence Statistics above and within two Amazon Rain Forest Canopies', *Boundary- Layer Meteorol.*, 94, 297-331.

Lumley, J.L. and Panofsky, H.A.: 1964, *The Structure of Atmospheric Turbulence*, John Wiley, New York [etc.], XI, pp. 239.

Maitani, T. and Shaw, R.H.: 1990, 'Joint Probability Analysis of Momentum and Heat Fluxes at a Deciduous Forest.' *Boundary-Layer Meteorol.*, 52, 283-300.

Mason, P.J. and King, J.C.: 1985, 'Measurements and Predictions of Flow and Turbulence over an Isolated Hill of Moderate Slope.', *Q.J.R.Meteorol.Soc.*, 111, 617-640.

Mazzoni, R.: 1996, *Turbulenzstruktur im gestörten Nachlauf einer künstlichen Oberflächenmodifikation. Ein Feldexpe-*

riment, Dissertation, ETH Zürich, Zürich, 133 pp.

McNider, R.T.: 1982, 'A Note on Velocity Fluctuations in Drainage Flows.' *J.Atm.Sci.*, 39, 1658-1660.

Nappo, C.J.: 2002, *An Introduction to Atmospheric Gravity Waves*, Academic Press, Amsterdam [etc.], 276 pp.

Panofsky, H.A. and Dutton, J.A.: 1984, *Atmospheric Turbulence - Models and Methods for Engineering Applications*, John Wiley, New York [etc.], 397 pp.

Peltier, L.J., Wyngaard, J.C., Khanna, S. And Brasseur, J.: 1996, 'Spectra in the Unstable Surface Layer.' *J.Atm.Sci.*, 53(1), 49-61.

Percival, B.D. and Walden, T.W.: 2000, *Wavelet Methods for Time Series Analysis*, Cambridge Univ. Press, Cambridge, 594 pp.

Porch, W.M., Clements, W.E. and Coultier, R.L.: 1991, 'Nighttime Valley Waves.' *J.Appl.Sci.*, 30, 145-156.

Rannik, Ü. and Vesala, T.: 1999, 'Autoregressive Filtering versus Linear Detrending in Estimation of Fluxes by the Eddy Covariance Method.' *Boundary-Layer Meteorol.*, 91, 259-280.

Raupach, M.R. and Finnigan, J.J.: 1997, 'The Influence of Topography on Meteorological Variables and Surface-Atmosphere Interactions', *J.Hydrol.*, 190, 182-213.

Raupach, M.R., Finnigan, J.J., Brunet, Y: 1989, 'Coherent eddies in vegetation canopies.' 4th Proc. Australasian Conf. Heat Mass Transfer, May 9-12, 1989, Christchurch, New Zealand, pp.75-90.

Raupach, M.R.: 1988, 'Canopy Transport Processes', In: W.L. Steffen and O.T. Denmead (ed.), *Flow and Transport in the Natural Environment: Advances and Applications*, Springer, Berlin [etc.], pp. 95-127.

Raupach, M.R. and Thom, A.S.: 1981, 'Turbulence in and above Plant Canopies', *Ann.Rev.Fluid Mechanics*, 13, 97-129.

Rotach, M.W., Calanca, C., Vogt,R., Steyn, D.G., Graziani, G., Andretta, M., Christen, A., Cieslik, S., Conolly, R., Galmarini, S., van Gorsel, E., Gurtz, J., Kadygrov, E., Miller, E., Neininger, B., Rucker, M., Weber, H., Weiss, A., de Wekker, S. and Zappa, M.: 2002, 'The Turbulence Structure and Exchange Processes in an Alpine Valley: The MAP-Riviera Project', submitted to *Bull.Amer.Soc.*

Rotach, M.W., Calanca, C., Vogt, R., Steyn, D.G., Graziani, G. and Gurtz, J.: 2000, 'The Turbulence Structure and Exchange Processes in an Alpine Valley: the MAP-Riviera Project', *Ninth Conference on Mountain Meteorology, Aspen, Co.*, Aug, 7-11, 2000, American Meteorological Society,45 Beacon St., Boston, MA, pp. 130-131.

Schmid, H.P. and Rotach, M.W.: 1997, *Grenzschichtmeteorologie*, ETH Zürich, Zürich, 114 pp.

Shaw, R.H., Brunet, Y., Finnigan, J.J. and Raupach, M.R.: 1995, 'A Wind Tunnel Study of Air Flow in Waving Wheat: Two Point Velocity Statistics.' *Boundary-Layer Meteorol.,* 76, 349-376.

Shaw, R.H. and Zhang, X.J.: 1992, 'Evidence of Pressure-Forced Turbulent Flow in a Forest.' *Boundary-Layer Meteorol.*, 58(3), 273-288.

Shaw, R.H., Tavanger, J. and Ward, D.P.: 1983, 'Structure of the Reynolds Stress in a Canopy Layer.' *J.Clim.Appl. Meteorol.*, 22(11), 1922- 1931.

Shaw, R.H., Silversies, R.H. And Thurtell, G.W.: 1974, 'Some Observations of Turbulence and Turbulent Transport

Within and Above Plant Canopies.' *Boundary-Layer Meteorol*., 5, 429-449.

Sorbjan, Z: 1989, *Structure of the Atmospheric Boundary Layer*, Prentice Hall, Englewood Cliffs (N.J.) [etc.], XVI, pp. 317.

Stone, G.L. and Hoard, D.E.: 1989, 'Low-Frequency Velocity and Temperature Fluctuations in Katabatic Valley Flows', *J.Appl.Meteorol.*, 28, 477-488.

Stull, R.B.: 1988, '*An Introduction to Boundary Layer Meteorology*', Kluwer Academic Publ., Dordrecht [etc.], 2nd repr., XII, Frontis, 666 pp.

Stull, R.B.: 2000, '*Meteorology for Scientists and Engineers*', Brooks/Cole, Pacific Grove, Calif., 2nd ed., 502 pp.

Su, H.B., Shaw,R.H., PawU, K.T., Moeng, C.H. and Sullivan, P.P.: 1998, 'Turbulent Statistics of Neutrally Stratified Flow Within and Above a Sparse Forest from Large-Eddy Simulation and Field Measurements', *Boundary-Layer Meteorol*., 88, 363-397.

Taylor, P.A. and , H.W.: 1987, 'The Askervein Hill Project: Overview and Background Data.' *Boundary-Layer Meteorol*., 539, 15-39.

Torrence, C. and Compo, G.P.: 1998, 'A Practical Guide to Wavelet Analysis', *Bull.Am.Met.Soc*., 79(1), 61-78.

Townsend, A.A.: 1961, 'Equilibrium Layers and Wall Turbulence.' *J.Fluid.Mech.*, 11, 87-120.

Vogt, R.: 1995, 'Theorie, Technik und Analyse der experimentellen Flussbestimmung am Beispiel des Hartheimer Kiefernwaldes', Dissertation, University of Basel, Basel, 101 pp.

Whiteman, C.D.: 1990, 'Observations of Thermally Developed Wind Systems in Mountainous Terrain', In: W. (ed.), *Atmospheric Processes over Complex Terrain*, 23, American Meteorological Society, Boston, MA, pp. 5-42.

Whiteman, C.D. and Allwine, K.J.: 1989, 'Deep Valley Radiation and Surface Energy Budget Microclimates. Part I: Radiation.' *J.App.Meteorol*., 28, 414-426.

Wood, N.: 2000, 'Windflow over Complex Terrain: A Historical Perspective and the Prospect for Large-Eddy Modelling.' *Boundary-Layer Meteorol*., 96, 11-32.

Wyngaard, J.C. and Cote, O.R.: 1972, 'Cospectral Similarity in the Atmospheric Surface Layer.' *Q.J.R.Meteorol.Soc*., 98, 590-603.

Zhang, C., Shaw, R.H. And PawU, K.T.: 1992, 'Spatial Characteristics of Turbulent Coherent Structures Within and Above an Orchard Canopy' In: S.E.Schwartz and W.G.N.Slim (coordinators), *Precipitation Scavening and Atmosphere-Surface Exchange*, Vol. 2, Hemisphere Publishing Co., Washington, DC, pp. 741-751.

Zhuang, Y. And Amiro, B.D.: 1994, 'Pressure Fluctuations during Coherent Motions and Their Effects on the Budgets of Turbulent Kinetic Energy and Momentum Flux Within a Forest Canopy. *J.Appl.Meteorol.*, 33, 704-711.